University of Freiburg

Faculty of Environment and Natural Resources

in cooperation with

Faculty of Engineering

‘Application of an innovative method (aerial infrared thermography) for the energetic evaluation of existing buildings’

Master thesis submitted in partial fulfilment of the requirements for the Degree of Master of Science in Renewable Energy Engineering and Management

by

Nirav Ashvinbhai Patel

Matriculation Number: 4967728

UNI FREIBURG

REM M.Sc. Renewable Energy Engineering and Management

DLR Institute of Solar Research

First Examiner: Prof. Dr. Hans-Martin Henning

Second Examiner: Prof. Dr. Bernhard Hoffschmidt

Scientific Supervisor: Philip Groesdonk, M.Sc.

Freiburg i.Br.,

Date of submission: 31.05.2023

Declaration of own work

I hereby certify that the thesis titled “Application of an innovative method (aerial infrared thermography) for the energetic evaluation of existing buildings” is entirely my original work except where otherwise indicated. I am aware of the University’s regulations concerning plagiarism, including those concerning disciplinary actions that may result from plagiarism. Any use of other authors’ works, in any form, is properly acknowledged at their point of use.

Freiburg i.Br., May 31, 2023 — Nirav Ashvinbhai Patel

Place, Date — Name

Acknowledgement

Throughout my thesis, I have received tremendous support and help from various people. I want to start by thanking my scientific supervisors, Mr. Philip Groesdonk and Dr. Benedikt Kölsch, at the host institution, DLR Institute of Solar Research, for whose knowledge and expertise helped steer the thesis in the right direction. I am grateful to Prof. Dr. Hans-Martin Henning, the academic advisor of my thesis, who guided me throughout the thsis to ensure that the academic requirements were fulfilled. I would also like to thank Prof. Dr. Bernhard Hoffschmidt who was also very kind to offer to be the second academic supervisor and showed great interest in my work.

I would like to extend my heartfelt gratitude to the entire team who has been involved in the completion of this thesis. Your contributions, whether big or small, have made a significant impact and have greatly enriched the quality of this work. Thank you for your commitment, expertise, and valuable insights throughout this journey. I also appreciate the help and support from my peers Harshvadan, Marmik, Mohak and Katharina who have provided valuable support and collaboration throughout the course of this thesis.

I would like to express my deepest gratitude to my friends and family for their unwavering support, encouragement, and understanding throughout the completion of this thesis. Your belief in my abilities, words of encouragement, and constant motivation have been invaluable. Thank you for being there for me, providing a strong support system, and celebrating both the successes and challenges of this academic endeavor with me. Your love and presence have made this journey all the more meaningful and fulfilling.

Abstract

The building sector's high share of energy consumption for heating is a global concern, as it contributes significantly to greenhouse gas emissions. Poorly insulated building envelopes are the primary cause of energy loss, and it is challenging to measure a building's energy performance on a large scale to identify weak points and possible renovation options. Traditional methods like the heat flux meter (HFM) require long measurement times and large manpower, making them impractical for large-scale use. Therefore, this master thesis deals with using non-contact drone-based infrared thermography to evaluate the energy performance of buildings on a large scale. The method offers the potential for a fast, large-scale, and automatable inventory that can contribute to resource-efficient modernization of the building stock. This thesis presents the principle of drone-based dynamic quantitative infrared thermography and its practical application on an exemplary building complex. The methodology involves generating a time series of surface temperature for each building surface based on several measurement flights during one night. The presented research applies the technology to calculate U-values and compare them to reference values acquired through conventional heat flux plate measurements. An important aspect of the thesis is the reduction of errors in the infrared camera measurement. The potential of a reference blackbody camera correction approach to solve the problem is investigated. The findings of the study demonstrate the effectiveness of the proposed method in identifying weak points and possible renovation options as well as accuracy issues. All in all, the thesis presents the development status of the proposed method and its potential for further development.

Table of contents

List of Figures

List of Tables

List of Acronyms

BB	Blackbody
BRDF	Bidirectional Reflectance Distribution Function
CHP	Combine Heat and Power
CHTC	Convective Heat Transfer Coefficient
DLR	Deutsches- Zentrum für Luft- und Raumfahrt / German Aerospace Center
FPA	Focal Plane Array
GPS	Global Positioning System
HFM	Heat Flux Method
HF	Heat Flux
IR	Infrared
IRT	Infrared Thermography
LWIR	Long-wave Infrared
MWIR	Mid-wave Infrared
NDT	Non-destructive Testing
NTC	Negative Temperature Coefficient
NUC	Non-uniformity Correction
RMSE	Root-mean-square Error
SWIR	Short-wave Infrared
TIR	Thermal Infrared Sensor
UAV	Unmanned Aerial Vehicle
U-value	Overall Heat Transfer Coefficient / Thermal Transmittance

Nomenclature

Term	Description	Unit
A	Area	m^2
c	Specific heat capacity	$\mathrm{J}\ /\ (\mathrm{kg\ K})$
c_0	Speed of light in a vacuum $= 2.998 \times 10^8$	$\mathrm{m/s}$
d	Thickness	m
d	Distance	m
E_i	Incident irradiance	$\mathrm{W/(m^2 sr)}$
g	Gravitational acceleration	$\mathrm{m/s^2}$
h	Planck's constant $= 1.381 \times 10^{-23}$	$\mathrm{J/K}$
h	Height	m
h_c	Convective heat transfer coefficient	$\mathrm{W/(m^2 K)}$
h_r	Radiative heat transfer coefficient	$\mathrm{W/(m^2 K)}$
k_B	Boltzmann's constant $= 6.626 \times 10^{-34}$	Js
k	Thermal conductivity	$\mathrm{W/mK}$
L	Radiance	$\mathrm{W/(m^2 sr)}$
L_BB	Blackbody radiance	$\mathrm{W/(m^2 sr)}$
L_T	Object's radiance at surface temperature	$\mathrm{W/(m^2 sr)}$
q	Density of heat flow rate	$\mathrm{W/m^2}$
R	Thermal resistance	$\mathrm{(m^2 K)/W}$
T	Temperature	K
T_BB	Blackbody surface temperature	K
T_cam	Camera body (housing) temperature	K
$T_\mathrm{refl,out}$	Outside apparent reflected temperature	K

$T_{\text{wall,in}}$	Inside wall surface temperature	K
$T_{\text{wall,out}}$	Outside wall surface temperature	K
$T_{\text{S,ref,meas,NTC}}$	Reference body temperature measured with NTC sensor	K
$T_{\text{S,ref,meas,IR}}$	Reference body temperature measured with IR camera	K
U	Overall heat transfer coefficient	$\text{W}/(\text{m}^2\text{K})$
v	Local wind speed	m/s

Greek letters

α	Absorptivity	-
β	Spectral response of IR camera	-
ε	Emissivity	-
λ	Wavelength	m
ρ	Density	kg/m^3
ρ	Reflectivity	-
σ	Stefan-Boltzmann constant $= 5.67 \times 10^{-8}$	$\text{W}/(\text{m}^2\text{K}^4)$
τ	Transmissivity	-
Φ	Heat flow rate	W
θ_i, ϕ_i	Direction of incident radiation	-
θ_r, ϕ_r	Direction of reflected radiation	-
ϕ	Relative humidity	%

Subscripts

atm	Atmospheric	-
BB	Blackbody	-
CO_2	Carbon dioxide	-

cv	Convection	-
env	Environment	-
H_2O	Water vapour	-
len	Lens	-
obj	Object	-
rad	Radiation	-
refl	Reflected	-
s	Surface	-
tot	Total	-
u	Upwelled	-

1 Introduction

1.1 Motivation

Buildings are an integral part of our everyday lives, and we spend a major part of our days in them, whether at home, at work, or during our spare time. Buildings are therefore the single largest energy consumer in the world. Heating, cooling, and domestic hot water account for 80% of the primary energy that we, as citizens, consume. In the EU, the building sector accounts for 40% of the total energy consumption and 36% of the total greenhouse gas emissions. Therefore, improving energy efficiency in buildings has a key role to play in achieving the ambitious goal of carbon neutrality by 2050, set out in the European Green Deal [1]. The majority of the energy used in the building sector is generated by the combustion of fossil fuels such as coal, petroleum, and gas. Thus, efficiency measures such as energy-efficient building renovations, but also changes in energy sources are critical to the success of the energy or heat transition. It is accepted that coordinated efforts by governments and policymakers around the world are essential to fully realize the potential for reducing energy demand, as current energy-efficiency policies and using the technologies already in place would not be sufficient to solve the issue [2].

To start with, the current state of the building stock needs to be assessed due to the performance gap in existing buildings. To forecast the energy performance of buildings, numerous calculation techniques and software tools have been developed. A number of studies have shown the gap between the energy performance of real buildings and the simulated performance [3], with clear implications for the efficiency of energy-saving practices, the estimation of heating and cooling loads, or policy prioritization [4]. This difference is frequently referred to as a "performance gap," and it depends on several factors, including the thermophysical properties of the building, occupant behavior and use of technology, and a lack of knowledge and skills [3]. A number of sensitivity analysis studies have shown that one of the most important parameters in the estimation of building performance is the thermophysical properties of the building, such as thermal resistance and U-value [5–7].

High-quality and reliable data about the status quo is required to analyze existing buildings. The current state-of-the-art methods to evaluate U-value mainly rely on on-site measurements by experts, where sensors need to be installed inside and outside building surfaces, which is time and cost intensive and also causes inconvenience to the inhabitants. To address these limitations in existing measurement methods, an aerial (drone-based) infrared thermography (IRT) based external measurement method is

tested, and a workflow is developed for the large-scale application presented in this thesis. The problem statement and research objectives of his thesis are described in the following section.

1.2 Problem Statement and Research Objectives

As described by Fokaides and Kalogirou [8], an internal IRT measurement method has shown great potential to measure the U-value of the building wall. However, this method has limitations like a long measurement time, high costs, a large manpower requirement, and a small measurement region compared to external IRT methods. To develop a less intrusive and more accurate method for measuring the in-situ U-value of opaque wall assemblies, researchers have created approaches that use infrared cameras for data collection also from the outside [9]. Consequently, this study emphasizes the practical application of drone-based external infrared thermography to quantitatively assess the U-values of building complexes and compare them with conventional, well-established methods. The following objectives are defined in this thesis:

1. Check the practical applicability of the existing dynamic U-value measurement method using external IRT
2. Automated data evaluation from drone-based external infrared thermography
3. Evaluation of drone-based external infrared (IR) thermographic measurements to determine the U-value of an exemplary building
4. Error reduction in the infrared camera measurements

The overarching goal of this thesis is to determine the practical applicability of aerial (drone) infrared thermography for the energetic evaluation of existing buildings. Furthermore, the potential for further development of this method will be explored and discussed.

The remainder of the thesis is structured as follows**: Chapter 2** overviews the theory and literature studied for this thesis and presents the state-of-the-art and existing infrared thermography measurement methods to evaluate the U-value**. Chapter 3** describes the experimental setup for data collection and explains the methodology used in the study**. Chapter 4** presents the results obtained after applying the methodology to analyze thermal images for the final U-value measurement. **Chapter 5** concludes the results and research objectives and lists the key findings of the thesis.

2 Theory and State-of-the-Art

This chapter introduces the fundamental terms and topics needed to put the work into context. To begin, Section 2.1 describes the heat energy flows in building envelopes. Then, the working principle of infrared thermography and infrared cameras, in general, is described in Section 2.2. To the last, Section 2.3 reviews the state-of-the-art U-value measurement methods and infrared thermographic methods.

2.1 Heat Energy Flows in Buildings

Building engineering physics deals principally with the flows of energy, both natural and artificial, within and through buildings. This field comprises a unique mix of heat and mass transfer physics, materials science, meteorology, construction technology, and human physiology necessary to solve problems in designing high-performance buildings. In building physics, heat transfer is one of the important phenomena, along with moisture, sound, and light. Whenever an object is at a temperature different from its surroundings, heat flows from hot to cold [10].

Heat flow can occur through three mechanisms: conduction, convection, and radiation. Which are briefly discussed in the following paragraphs.

Thermal conduction is the diffusion of heat energy within a solid material from molecule to molecule as a result of a temperature difference across it. Heat will tend to flow from the particles at a higher temperature to the adjacent particles at a lower temperature. Conduction is one of the main heat transfer mechanisms in buildings where internal heating or cooling can be lost to the outside environment, causing high energy consumption, high carbon emissions, high operating costs, and human discomfort. In general, conductive heat transfer through the homogeneous body can be calculated from Fourier's law [11].

$$q = \frac{kA\partial T}{d}, \tag{1}$$

where k is the body's thermal conductivity, A is the area of the body, ∂T is the temperature difference across the body, d is the body's thickness.

Thermal convection is the transfer of heat from one place to another by the movement of fluids. The rate of convective heat transfer is observed to be proportional to a convective heat transfer coefficient and the temperature difference expressed by Newton's law of cooling [12]

$$Q = h_{\mathrm{c}} A (T - T_{\mathrm{f}}), \tag{2}$$

where Q is the convective heat transfer per unit time, h_{c} is the heat transfer coefficient, A is the area of the object, T is the object's surface temperature, and T_{f} is the fluid temperature. The heat transfer coefficient is typically not uniform across a surface and depends on flow conditions, thermophysical properties, surface geometry, and dimensions. Convection is classified into two groups: natural (or free) convection and forced convection, depending on how the fluid motion is initiated. Natural convection can be wind-driven, or buoyancy-driven [11]. For standard application in the building energy modelling, h_{c} values are taken from ISO 6946 [13].

Thermal radiation is the movement of heat through space as electromagnetic waves. Therefore, it primarily occurs in vacuum and gases. All bodies at temperature $T > 0$ K emit energy via thermal radiation, and they also absorb the thermal radiation emitted by their surroundings. The difference in the total amount of emitted and absorbed radiation by a body at any given time may result in a net heat transfer, which will result in a temperature change in the body. A standard example of heat transfer by radiation occurs between the Sun and the Earth. There is no other way for heat to travel between these two objects because they are separated by a vacuum [14].

For simplification, an ideal absorber and emitter can be assumed, which absorbs all incident radiation and emits the maximum amount of energy in all directions and at each wavelength. This kind of perfect absorber-emitter is called a blackbody. For a blackbody at temperature T, the spectral density of heat flow rate Q_λ is explained by Planck's law. The following equations for thermal radiation are taken from [10].

$$Q_\lambda(\lambda, T) = \frac{2hc^2}{\lambda^5 \, exp\left(\frac{h_{\mathrm{c}}}{\lambda k_{\mathrm{B}} T}\right) - 1}, \tag{3}$$

where c is the speed of light in a vacuum, h is Planck's constant, and k_B is Boltzmann's constant. Figure 1 shows the spectral density of heat flow rate for three different temperatures (5800 K, 1000 K, 300 K).

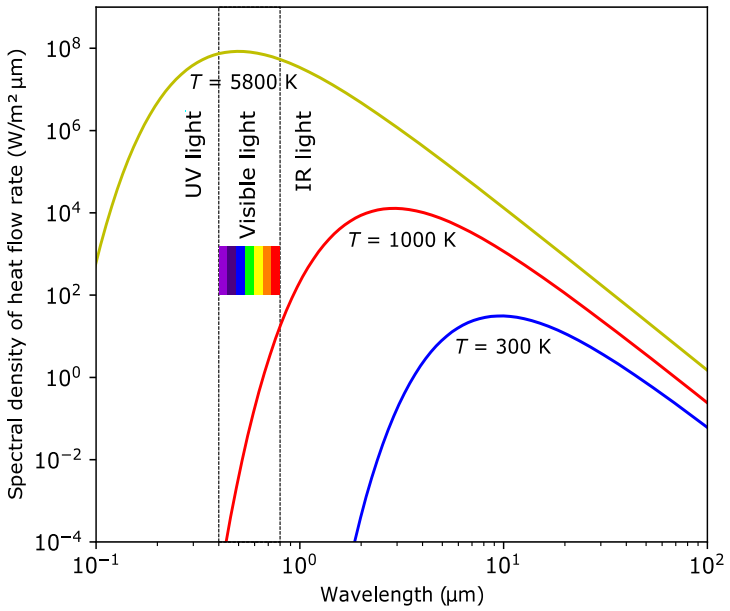

Figure 1. Spectral density of heat flow rate at 5800 K, 1000 K, and 300 K [15].

The total density of heat flow rate for a blackbody, known as the Stefan-Boltzmann law, is determined by integrating Plank's law over all wavelengths

$$q(T) = \sigma A T^4, \tag{4}$$

where σ is called the Stefan-Boltzmann constant and, A is radiating surface area. This is only true for the ideal blackbody. For surfaces which are not blackbodies, one has to consider the emissivity factor $\varepsilon(\gamma)$.

$$q(T) = \sigma \varepsilon A T^4. \tag{5}$$

Whereas in reality, in real bodies some amount of the incident radiation is absorbed, some is transmitted and the rest is reflected. These are three physical quantities absorptivity α, reflectivity ρ and transmittivity τ. Their value ranges are $0 \leq \alpha(\lambda), \rho(\lambda), \tau(\lambda) \leq 1$. The following equation describes how thermal radiation interacts with energy exchange

$$\alpha(\lambda) + \rho(\lambda) + \tau(\lambda) = 1. \quad (6)$$

Up to this point, the discussion has revolved around the radiation emitted by a single body. Let us now focus on the issue of radiative exchange between two or more bodies. In building physics, we are interested in net radiation exchange between the wall surface and its surrounding environment. The net radiation exchange in the room for each pair of objects is very small because they are in the same environment, and the majority of net radiation exchange happens between the wall surface and the environment [10]. In this case, the radiation heat transfer is described as,

$$q = \sigma \varepsilon_{\text{wall}} (T_{\text{s}}^4 - T_{\text{env}}^4), \quad (7)$$

where $\varepsilon_{\text{wall}}$ is wall emissivity, T_{s} is wall surface temperature and T_{env} is environmental (i.e. background) temperature for which $\sigma * \varepsilon_{\text{wall}} * T_{\text{env}}^4$ is the radiation absorbed by the wall. Using Newton's law of cooling, the radiative heat exchange can be written as the product of radiative heat transfer coefficient (h_{r}) and temperature difference,

$$q = h_{\text{r}} (T_{\text{s}} - T_{\text{env}}). \quad (8)$$

To summarize this section, the introduction of heat transfer in building envelopes through conduction, convection, and radiation has been presented. The concept of U-value has been introduced as a measure of the overall heat transfer rate in building envelopes. In other words, a component's U-value evaluates how well or poorly heat is transmitted from the warmer to the colder side of the component. Now, we are one step closer to understanding how U-value is measured in building envelopes. In the following section, the working principle of an IR camera is explained which allows readers to understand the most influencing parameters for the accurate measurement of surface temperature with infrared thermography.

2.2 Infrared Thermography

Infrared (IR) thermography is the field of collecting and analyzing thermal data using non-contact thermal imaging devices such as infrared cameras. IR camera is a type of advanced sensor that detects the infrared radiation received and transfers it into an electronic signal. Depending on the type of analysis (quantitative or qualitative), this signal can then be post-processed into digital signals in a number of ways. Temperature is one of the most commonly measured physical quantities in infrared thermography.

In this thesis, a quantitative approach has been chosen, wherein surface temperatures are measured using IR cameras. IR cameras measure infrared radiation received by the detector and then convert the received energy into temperature values. However, not all of the radiation received comes from the target object alone, but also from its surroundings and the atmosphere. I.e., the temperature value given out by the camera would be the radiation temperature of the influx, but it is not, because of the following. For an accurate measurement of an object's surface temperature, both surrounding and atmospheric radiation sources must be eliminated; this process is known as compensation [16]. The radiance at the camera lens is the total of the three sources of radiance L_{tot}: the emitted radiance from the target object L_{obj}, the ambient radiance reflected by the object L_{refl} and the radiance caused by the atmosphere in between sensor and object L_{atm}. The atmosphere also influences L_{obj} and L_{refl}.

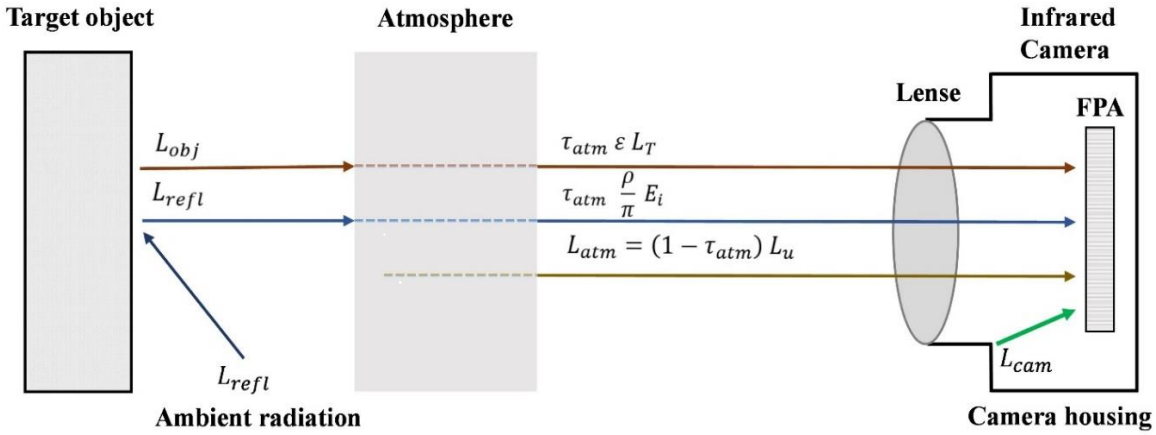

Figure 2. Radiance received by the camera lens and the FPA (detector) of the IR camera [15].

As shown in Figure 2, the total radiance L_{tot} received by the camera lens is described as

$$L_{\text{tot}} = L_{\text{obj}} + L_{\text{refl}} + L_{\text{atm}}. \tag{9}$$

Figure 2 also illustrates that the focal plane arrays (FPA) of the IR camera receive not only L_{tot}, but also a large amount of radiation from the camera housing L_{cam}. The majority of infrared cameras are calibrated at room temperature. The camera housing temperature is kept constant at room temperature during calibration, and the radiation from the camera housing is measured and adjusted in the calibration model [17].

The first source is the radiation coming from the target object. However, not all the emitted radiation by the target object is received by the IR camera; some is absorbed by the atmosphere as a function of the transmittance of the atmosphere (τ_{atm}). Thus, the radiation of the target object can be expressed as an equation

$$L_{\mathrm{obj}} = \tau_{\mathrm{atm}}\, \varepsilon\, L_{\mathrm{T}}, \tag{10}$$

where ε is surface emissivity, L_{T} is blackbody radiance at surface temperature. As we know, real bodies have a reflectivity greater than zero. Thus, the second component is the reflected radiation coming from the surroundings and reflected by the atmosphere. The reflected radiation is a function of the angle of incidence. The total reflected radiance is L_{refl} and according to Nicodemus et al. [18], reflected radiance $L_r(\theta_r, \phi_r)$ is derived as:

$$L_r(\theta_r, \phi_r) = \int_{\omega_i} L_i(\theta_i, \phi_i)\, f_r(\theta_i, \phi_i;\, \theta_r, \phi_r)\, d\Omega_i, \tag{11}$$

where $f_r(\theta_i, \phi_i\, ;\, \theta_r, \phi_r)$ is the BRDF (bidirectional reflectance distribution function) also known as concentration of reflectance. Also, since f_r depends only upon directions, the geometry of the incident and exiting radiation can be represented by a simple polar diagram, as shown in Figure 3.

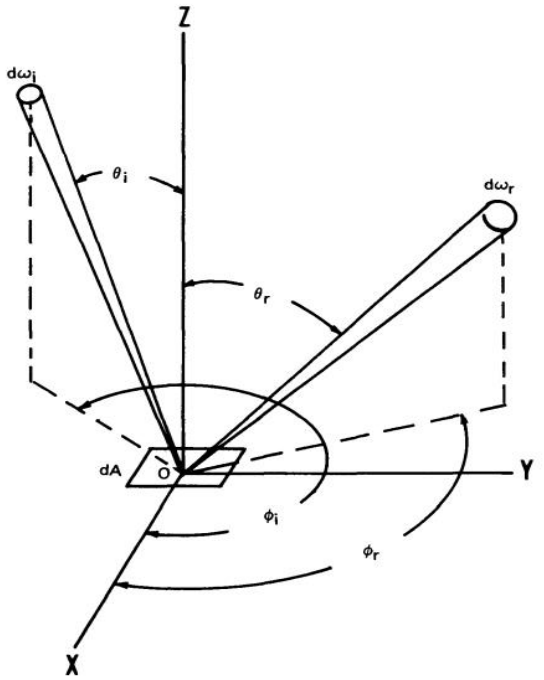

Figure 3. The geometry of incident and reflected elementary beams [18].

$d\Omega_i$ is projected solid angle which is the product of an element of solid angle $d\omega_i$ with the cosine of the angle θ between the normal to the surface and the direction associated with $d\omega_i$ by $d\Omega_i$ ($d\Omega_i = \cos\theta \; d\omega_i$). Incident radiance is $L_i(\theta_i, \phi_i)$. In simplification, surfaces are often considered to behave like a perfectly diffuse or "Lambertian" surface which means the reflected radiance is isotropic so that L_r is a constant, regardless of how it is irradiated it is the same value for all the directions of reflection (θ_r, ϕ_r) [18]. From equation (11) we can derive the equation as

$$L_r = f_r \int_{\omega_i} L_i(\theta_i, \phi_i) \; d\Omega_i = f_r \, E_\mathrm{i}, \tag{12}$$

where E_i is incident irradiance. In terms of the perfectly diffuse reflectance ρ, which is the fraction of the total incident flux that is reflected isotopically (iso-radiance rays) in all directions f_r can be written as $\frac{\rho}{\pi}$ [18]. If we additionally consider atmospheric transmissivity (τ_atm), equation (12) can be written as

$$L_\mathrm{refl} = \tau_\mathrm{atm} \; \frac{\rho}{\pi} \, E_\mathrm{i}. \tag{13}$$

The third source is the infrared radiation from the atmosphere, where $\varepsilon_{\mathrm{atm}} = (1 - \tau_{\mathrm{atm}})$ is the emittance of the atmosphere and L_{u} is upwelled radiance of the atmosphere between surface and camera [19]. Radiation from the atmosphere can be expressed as

$$L_{\mathrm{atm}} = (1 - \tau_{\mathrm{atm}})\, L_{\mathrm{u}}. \tag{14}$$

Substituting equations (10) (13) and (14) in (9), equation (15) can be obtained for the total radiance at the camera.

$$L_{\mathrm{tot}} = \tau_{\mathrm{atm}}\, \varepsilon\, L_{\mathrm{T}} + \tau_{\mathrm{atm}}\, \frac{\rho}{\pi}\, E_{\mathrm{i}} + (1 - \tau_{\mathrm{atm}})\, L_{\mathrm{u}}. \tag{15}$$

As seen in equation (15), parameters like object emissivity, ambient reflected radiance, and the transmissivity of the atmosphere are required for accurate temperature measurement. According to Schott, radiometric calibration of atmospheric effect in the thermal and reflected regions of the spectrum is also important to consider [20]. Which is described in the methodology Section 3.2.3. The transmissivity of an atmosphere depends on air temperature, distance from the camera to the object, and relative humidity. The object emissivity for standard materials can be taken from the literature [21]. Ambient reflected radiance can be measured using the aluminum foil method [22]. The other three parameters, namely air temperature, relative humidity, and camera-to-object distance, can be measured by additional sensors. Details about all measurements on-site are described in the measurement campaign section 3.1. In the following section, standard U-value measurement methods will be introduced. Then, different infrared thermographic methods for building analysis will be reviewed.

2.3 State-of-the-Art U-value Measurement Approaches

To increase the sustainability and performance of our buildings, it is crucial to understand and measure U-values. It is also known as thermal transmittance. U-value is a measure of the overall rate of heat transfer in building envelopes. In other words, a component's U-value evaluates how well or poorly heat is transmitted from the warmer to the colder side of the component. The slower or more difficult it is for heat to transfer through the component, the lower the U-value. Which indicates a high quality of insulation.

Baker [23] compared the pre-calculated and measured U-values for traditional buildings and stated how the assumed U-values used in modelling software are often conservative to account for this because they are overestimated and gives underperformance resulting in predictions. Li et al. [24] discussed that predetermined U-values are likely to be inappropriate for energy certification and for the economic evaluation of a retrofit. According to them, unnecessary and costly energy conservation measures are applied to the building. This can be improved by reliable and accurate measurements of the U-value.

2.3.1 Design Data Method based on ISO 6946

As you can guess from the name of this method, the design data of the building components are used to calculate the thermal resistance and thermal transmittance. The method applies to components and elements consisting of thermally homogeneous layers, which can include air layers. Design thermal values can be given as either design thermal conductivity or design thermal resistance. If thermal conductivity is given, the thermal resistance can be obtained, and vice-versa [13],

$$R_i = \frac{d_i}{k_i}, \tag{16}$$

where the index i indicates the selected layer of the component of the building envelope, R is the thermal resistance, d is the thickness of the material layer in the component and k is the design thermal conductivity of the material. The total thermal resistance R_{tot} of a plane building component between the environments on both sides consisting of thermally homogeneous layers perpendicular to the heat flow shall be calculated as

$$R_{\mathrm{tot}} = R_{\mathrm{si}} + R_1 + R_2 \ldots\ldots + R_n + R_{\mathrm{se}}, \quad (17)$$

where R_{tot} is the total thermal resistance, $R_1, R_2 \ldots R_n$ are the design thermal resistance of the layers, R_{si} is the internal surface resistance, and R_{se} is the external surface resistance. Table 1 shows the conventional surface resistances.

Table 1. Conventional surface resistances [13].

Surface resistance in m^2 K/W	**Direction of heat flow**		
	Upwards	**Horizontal**	**Downwards**
R_{si}	0.10	0.13	0.17
R_{se}	0.04	0.04	0.04

Typically, during the design phase of new construction, the U-value is calculated theoretically based on information that has been made available regarding the thermal resistance (R-value) for each layer of the wall assembly [25],

$$U = \frac{1}{R_{\mathrm{tot}}}. \quad (18)$$

However, for the existing buildings, design data is not available, especially for the older ones, and hence this method is not truly feasible [26]. In addition, if design data is available, the assumed and actual physical properties of the materials might be different due to the ageing and deterioration of the materials. These differences in physical properties result in changes in thermal resistance. Therefore, either laboratory or in-situ thermal transmittance measurement of the building envelope would be a reasonable approach. The following section describes how the heat flux meter method works to determine the U-value of a building envelope.

2.3.2 Heat Flux Meter Method based on ISO 9869-1

The heat flux meter method based on ISO 9869-1:2014 [27] is a commonly used and standard measurement method for calculating the U-value from the in-situ measurement of the building envelope. This method incorporates the use of on-site installation of temperature sensors and heat flux sensors on existing building walls. To save the measured dataset, all sensors are linked to a data logger. According to ISO 9869-1:2014, thermal resistance R can be calculated by using the average method, i.e., by calculating the ratio of the mean surface temperature difference over the mean density of heat flow rate,

$$R = \frac{\sum_{j=1}^{n}(T_{\text{wall,in } j} - T_{\text{wall,out } j})}{\sum_{j=1}^{n} q_j}, \tag{19}$$

where q_j is the heat flux passing through the spot measured at each time step i; n is the number of observations; $T_{\text{wall,in } j}$, $T_{\text{wall,out } j}$ are the internal and external surface temperature at each time step.

The heat flux (HF) plate sensor measures the passing heat flux through the building element. Exemplary HF plates from the company Hukseflux are presented in Figure 4. To get the positive HF reading, the red side faces the warmer environment and the blue faces the colder environment. These HF sensors are used in this thesis for reference measurements. More information about the HFP01 type of sensor can be found here [28].

Figure 4. HFP01 heat flux plate (HF sensors) [28].

All the sensors need to be calibrated before using for the measurement campaign, and their accuracy levels need to be compared with the ISO 9869-1:2014 guidelines. Also, the installation procedure for HF and temperature sensors is described in the same standard. The average method is based on the steady-state assumption that the energy storage in the wall remains constant during the measurement period. However, it is only possible if the temperature difference between the two ends remains constant

throughout the measurement. In reality, this is unlikely to occur, and thus the U-value is influenced by the storage effect. To minimize this effect, the following criteria are suggested [27]:

- the duration of the measurement exceeds 72 h;
- the analysis period is an integer multiple of 24 h;
- thermal resistance of the surface obtained at the end of the test should not differ by more than ±5% from the value obtained 24 h before;
- thermal resistance of the surface, obtained for an initial period representing a number of full days equal to two third of the duration of the measurement campaign, should not differ by more than 5% from the value calculated from an equally long period at the end of the campaign [27].

In addition, if the change in thermal resistance is greater than 5%, the storage effects have to be considered according to the method mentioned in ISO 9869-1:2014 [27], section 7.2, and Annex B, and the method suggested in the standard makes significant assumptions that the thermal mass may be calculated from the literature rather than in-situ measurements [3]. Furthermore, the steady-state assumptions are nearly impossible to achieve in reality.

In Annex-B of ISO 9869-1:2014 [27], dynamic methods are also proposed to overcome some of the limitations of steady-state approaches. The dynamic method helps when there is a significant variation in temperatures and heat flow rates. Also, the measurement time can be reduced compared to the steady-state regulations. The historical overview of the dynamic methods is described in [3]. The methodology and calculations stated in ISO 9869-1:2014 have many practical flaws, which restrict quick and reliable estimation of U-value. To overcome some of the limitations of the HFM method, methods using IR thermography have been developed, which are presented in the following section.

2.3.3 Methods Using Infrared Thermography

Infrared thermography (IRT) has gained popularity among non-destructive building diagnostic technologies, particularly with the rising concerns about energy minimization and low energy consumption in the building sector [29]. A qualitative approach using IRT has been shown to be an effective method in building construction. It is mainly used to detect voids and irregularities in the wall surface, investigate the structural element beneath the plaster, detect plaster delamination [30], detect moisture in the near-surface region [31], and a variety of other applications. In order to calculate U-values, a quantitative analysis is required. Quantitative analysis is not a trivial task, and researchers have been working on developing methods to accurately measure the wall surface temperature for the past few years. Before reviewing quantitative approaches using IR cameras, let us first understand the benefits of IRT over HFM in measuring U-value. They are listed in Table 2.

Table 2. Benefits of the IRT method over the HFM method to measure the U-value.

IRT-based U-value measurement method	**HFM-based U-value measurement method**
Whole façade measurement	Spot measurement
Non-contact measurement	Contact measurement
Non-destructive	Need of destruction (for rough surfaces)
Time-efficient	Time-consuming
Less manpower	More manpower

The assessment of the whole building façade is important in order to get an accurate U-value. In most existing buildings, an envelope has an inhomogeneous heat flow pattern due to heat bridges or the use of different materials in the envelope. The use of one or two HFM sensors on the wall surface can only provide information on a very small region of the whole façade. Therefore, accurate U-values valid for the whole building envelope cannot be measured by using the spot measurement, as they do not represent the whole envelope. On the other hand, in IR thermography, a thermal image of the whole envelope is taken, which provides detailed information about the complete envelope.

In the HFM method, going door to door in each building and room becomes a tedious task for the operator, resulting in a time-consuming job. The IRT method enables the scanning of multiple buildings in a short time, requiring less manpower while covering the wall surface area that the HFM method is unable to include in the measurement.

The HFM method is a pure contact measurement method, whereas the IRT method, thanks to the IR camera, is a non-contact measurement method. In the HFM method described in ISO 9869-1 [27], improper contact between the HF sensor and the wall causes significant errors in HF measurements. This kind of error is observed while analyzing the data measured for the reference U-value measurement and is described in section 4.5.1.

The IRT-based U-value measurement methods have evolved over time. For indoor measurements, an internationally standardized method exists, in which a stationary camera is positioned at the same place over several days [32]. The controlled environmental conditions are advantageous here. A measurement from the outside has potentially shorter recording periods, but the consideration of changing conditions is challenging. In the literature, methods are found that involve the use of stationary cameras recording a time series [33] as well as the utilization of mobile measurement devices where only one recording is used for each target [34–36].

In the past decade, researchers from all around the world have carried out significant developments. As described in a paper published during this thesis [37], Figure 5 shows an overview of various approaches discussed in this literature review, in which the thermal properties of building components are inferred from their recorded thermal radiation. Mostly U-values are targeted. Here, a brief review of the method's development is presented in this section.

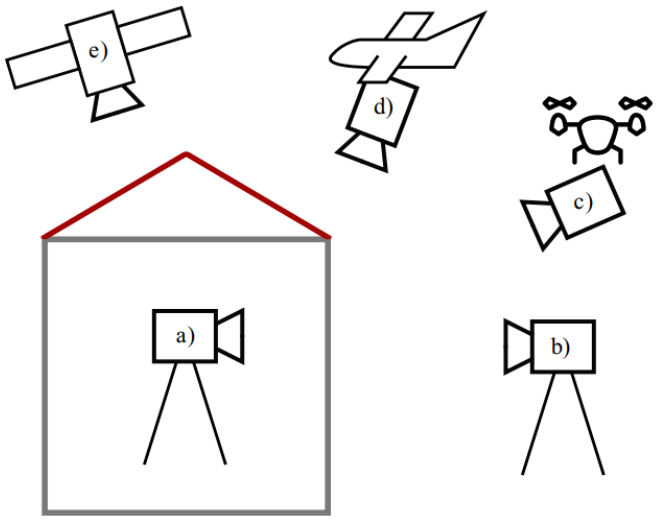

Figure 5. Different methods for thermographic investigation of buildings: a) stationary indoor, b) stationary outdoor, c) drone-borne camera, d) aerial thermography, e) satellite-based thermography [37].

The first study to quantitatively determine the U-value of a building envelope using internal IRT was performed by Madding [38] in 2008, using an internal IRT method and a testing procedure that was also mentioned in a couple of later studies [39, 40]. Madding describes the quantification of heat transfer by radiation and convection at inside walls using the indoor and outdoor air temperatures, the inside wall surface temperature, the apparent reflected temperature, and the inside wall surface emissivity. The proposed formula can be seen in the following equation

$$U = \frac{4\varepsilon\sigma\left(\frac{T_{\mathrm{wall,in}} + T_{\mathrm{refl,in}}}{2}\right)^3 \left(T_{\mathrm{wall,in}} - T_{\mathrm{refl,in}}\right) + h_{\mathrm{c,in}}\left(T_{\mathrm{wall,in}} - T_{\mathrm{air,in}}\right)}{T_{\mathrm{air,in}} - T_{\mathrm{air,out}}}, \tag{20}$$

where $T_{\mathrm{wall,in}}$ and $T_{\mathrm{refl,in}}$ are the inside wall surface temperature and reflected temperature respectively; $h_{\mathrm{c,in}}$ is the convective heat transfer of inside space; $T_{\mathrm{air,in}}$ and $T_{\mathrm{air,out}}$ are the inside and outside air temperatures. An important aspect of his model was the unity view factor inside the room as the surrounding walls have almost the same temperature. This method won't be feasible for external measurement work due to the significant difference in sky temperature compared to the surroundings.

The detailed study performed by Fokaides and Kalogirou in [8] shows the measurement of the overall heat transfer coefficient using an indoor IRT method and compared it with the traditional HFM method. Here, the only difference compared to Madding's [38] method is that they have used the third power of only the surface temperature rather than the third powers of mean inner surface temperature and reflected temperature, described as

$$U = \frac{4\varepsilon\sigma T_{\mathrm{wall,in}}^3\left(T_{\mathrm{wall,in}} - T_{\mathrm{refl,in}}\right) + h_{\mathrm{c,in}}\left(T_{\mathrm{wall,in}} - T_{\mathrm{air,in}}\right)}{T_{\mathrm{air,in}} - T_{\mathrm{air,out}}}. \tag{21}$$

The $h_{\mathrm{c,in}}$ was taken from ISO 6946 [13]. The R-value presented using the IRT approach, according to the authors [8], offers more accurate results because it takes into account radiative factors including emissivity and reflected ambient temperature. Reflected temperature is measured using crumpled and re-flattened aluminum foil, as described in ISO-18434-1 [41].

The authors [8] mentioned that the emissivity and reflected ambient temperature are the most influential parameters in the sensitivity analysis of surface temperature measurement. For instance, a deviation of

1 K in reflected ambient temperature can cause a 10% error in surface temperature calculation; however, this can be reduced significantly in the case of higher emissivity values, which are common in building envelopes. The authors [8] also stated that a small difference in surface temperature can result in a 100% error in the U-value calculation as the measurement time is much shorter when using the IRT method compared to the HFM method. The authors suggested that since IRT should ideally be performed at a steady state, measurements should be scheduled in the early mornings or overnight when surfaces are not exposed to solar radiation and when outdoor air temperature variations are minimal.

Overall, these studies have shown promise in terms of obtaining acceptable in situ U-value measurements using internal IRT. In recent years, external IRT has also been of interest to researchers despite its limitations compared to internal IRT. First, the exterior surfaces are significantly more influenced by climatic conditions than the internal surfaces, which are well controlled [8]. Second, nearby objects in the environment emit and reflect radiation onto the target, which is commonly uncontrollable [8]. Finally, in order to get reliable results, the outside convective heat transfer coefficient must be calculated based on the current weather conditions since it varies during measurement [42].

Schott et al. [35] conducted an aerial infrared survey to measure the roof surface temperature and net heat flux from the roof structure. The method described in this study accounts for atmospheric and emissivity effects on the thermogram data. The result shows that the qualitative approach tends to deliver misleading heat loss assessments, whereas the quantitative approach is largely free of this deficiency.

Albatici et al. [43] carried out a comprehensive study on the effects of thermal mass and cardinal direction of wall exposure on in-situ U-value measurements using external IRT. The authors used the truncated Jurge equation in the IRT model to get the $h_{c,out}$. The analysis showed that the standard deviation of U-values for north-facing light walls was significantly higher (37-50%) than for heavy walls (10.8-17.8%). The standard deviation ranges for south-facing walls were wider, ranging from 10.8% to 58.3% for light walls and 24.2% to 31.4% for heavy walls. The study also compared IRT and HFM results, concluding that deviations can vary significantly due to the influence of the cardinal direction of wall exposure (9.0-40%).

Dall'O' et al. [42] conducted several in-situ measurements to determine wall U-values in dwellings of varying construction using external IRT. The U-value was calculated using a simplified IRT method that included the Jurge equation, which considers the effects of radiation and convection. The results showed that deviations of IRT from theoretical values ranged from 1.7% to 154%, depending on wind speed and building construction. It is suggested to avoid the IRT measurements on rainy and sunny days.

Nardi et al. [39] published the results of U-value measurements for a well-insulated building envelope using the same method as described by Albatici et al. [43]. The U-values were analyzed against different indoor-outdoor temperature gradients, reflected temperatures, and outdoor-reflected temperature differences. Results were consistent with findings from Madding [38] and Fokaides et al. [8] due to the similarity of their governing equations. The study concluded that testing during overcast skies and larger indoor-outdoor temperature gradients is optimal.

Hui et al. [44] propose an innovative solution to target the building's efficiency using satellite thermal infrared (TIR) imaging to detect heat loss in the building sector. The method is still in the development stage yet, but it is certainly one step towards a futuristic approach to tackle the retrofit problem of inefficient buildings.

A laboratory-based study from Simões et al. [40] compared the results of three distinct surface temperature measurement methods using IR cameras. According to this study, the most reliable results were achieved by the method published by Fokaides et al. [8]. An important takeaway from this study is that the accurate U-value calculation depends on accurately reflected temperature, wind speed, and emissivity measurement.

The following boundary conditions have been established by researchers to compensate for the effects of environmental parameters in external quantitative IRT: The temperature difference between inside and outside should be at least 10 °C to have sufficient thermal heat flux through the envelope [8, 43, 45], outdoor air temperature variations 12 hours before the test should be less than 6 °C to approximate steady state conditions [43]. Furthermore, a local wind speed of less than 0.5 m/s near the building surface during the measurement and a free stream wind speed of less than 5 m/s are recommended [43, 46]. To avoid the influence of solar radiation, measurements should be taken in the early mornings (at least two hours before sunrise) or late evenings [43]. In general, skies should be overcast for 12 hours before the test to mitigate the effects of solar and sky radiation [8, 39, 42, 43]. Measurements should not be performed on days that are rainy or snowy, and surfaces should be dry for 24 to 48 hours before the test since moisture increases the heat conductivity of materials and promotes evaporative cooling [43, 45]. The majority of the literature suggests best results are obtained if quasi-steady state conditions are achieved 3-4 hours prior to IRT [8].

The collection of academic literature is showing some promise in using IRT as a quantitative approach for evaluating building envelope thermal performance. However, research to date is preliminary and many other conditions need to be tested. The majority of the studies were performed from the inside and

assumed steady-state conditions, which in reality is not true. External measurement of the building envelope is still in progress. However, in-situ U-value measurements of a wall assembly with drone-based external IRT were not investigated in the literature. Furthermore, no studies have evaluated the whole building with the drone-based IRT. To address the current gap in the literature, this study aims to assess the use of external IRT with a combination of flying a drone multiple times over the course of a night to create the drone-based dynamic quantitative infrared thermography to measure the U-value of the existing building while introducing some practical techniques to improve the accuracy of measurements. This is described in the following section.

3 Methodology and Experimental Application

The overall thermal transmittance measurement was carried out on the building complex of Hahn-Schickard in Villingen-Schwenningen. This section deals with the methodology of the procedure. In order to illustrate the practical relevance of the experimental application and to justify the selection of various options for action in the actual project implementation, the experimental application is presented directly in combination with the individual steps of the procedure. Figure 6 shows an overview that integrates drone-based quantitative infrared thermography into an overall concept for measurement data acquisition, analysis, and use. In the following, the HFM measurement campaign, the nighttime flight itself, the extraction of image textures for the exterior surfaces, the quantitative image analysis, and the calculation of the U-values will be discussed.

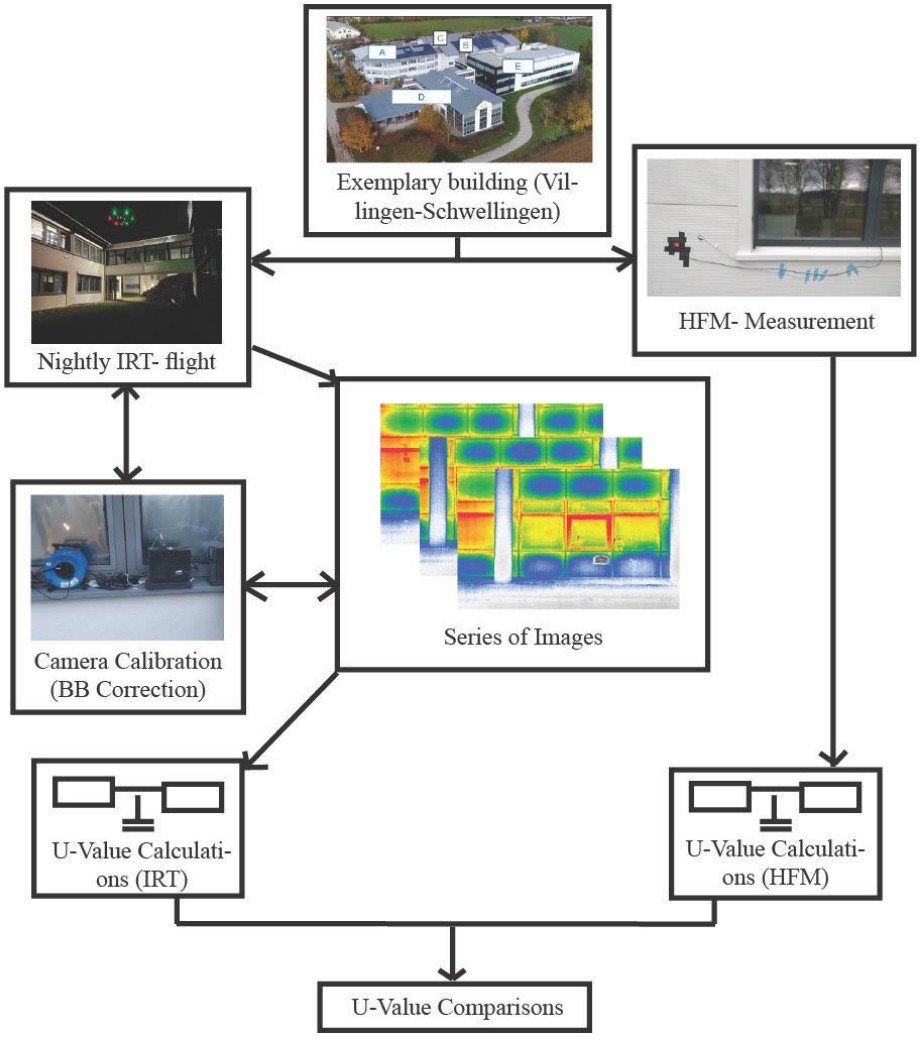

Figure 6. Overview of the method with integration into an overall concept.

3.1 Measurement Campaign

This chapter covers the experimental setup for HFM and IRT measurement. The data collection campaign for both methods is performed on an existing building, which is shown in Figure 7.

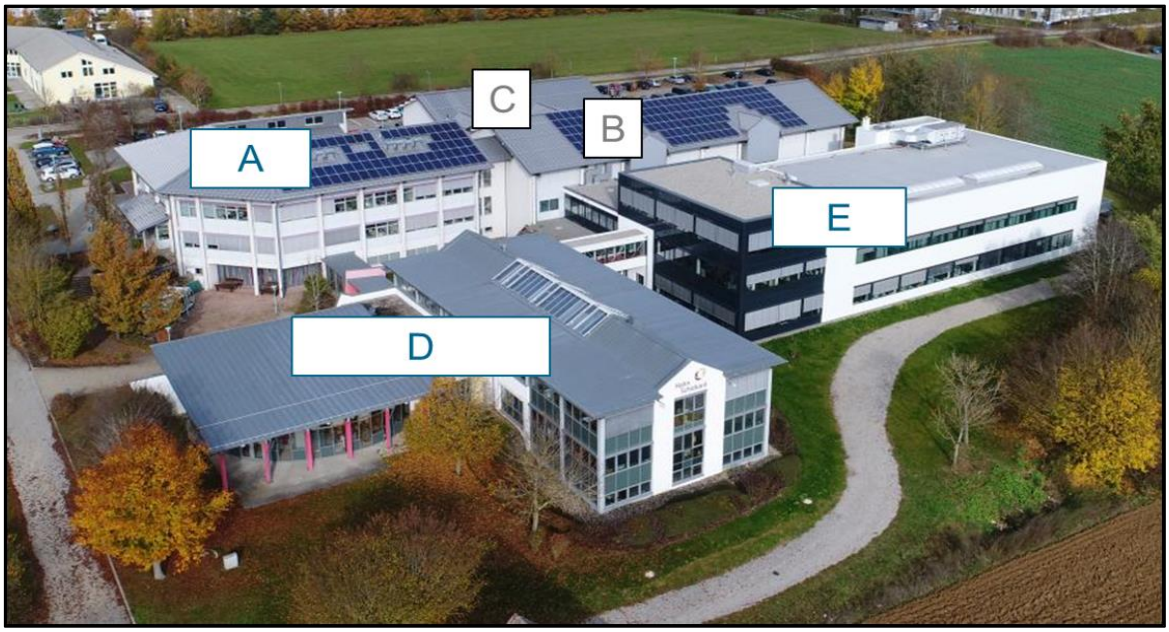

Figure 7. Hahn-Schickard, Villingen-Schwenningen (research institute building).

The complex has a heterogeneous structure in terms of age (construction between 1989 and 2019) and thus in terms of insulation quality, but also terms of surface materials. Therefore, this building is well suited to test the applicability of the process for different types of building components. At the same time, the location has little vegetation and hardly any surrounding buildings which makes it advantageous for flight planning. The years of construction, uses and surface area are listed in Table 3.

Table 3. Building details.

Building block	**Year of construction**	**Use**	**Surface area (m^2)**
A	1989	Offices and laboratories	1722
B	1989	Clean room	808
C	1989	CHP / Technology	883
D	1998	Offices	1386
E	2019	Office	1386
E	2019	Clean room	784

3.1.1 HFM Measurement Setup

The steady-state HFM method, mentioned in Section 2.3.2 , is selected as a reference method to measure the reference U-values of the building complex shown in Figure 7.

Figure 8. Heat flux sensors and temperature sensors installed at different places within the building. (a) block A outside PVC wall, (b) block D outside roof, (c) block E outside PVC wall, (d) block D outside plaster wall.

As shown in Figure 8, multiple heat flux and temperature sensors were placed on different walls of blocks A, D, and E. This choice was made because these three blocks have most of the offices, which are easy to access compared to clean rooms and laboratories. Two HF sensors were placed at each location within the building, one at the inner part of the wall and the other at the outer part of the wall. Detailed floor plans with the sensors' location are shown in the appendix A.1, A.2, and A.3. As recommended by ASTM C 1046-95 [47], a thermally conductive paste is used to provide better thermal contact between the sensor and the wall. NTC sensors are used for the wall surface temperature and inside air temperature. A detailed description of sensors and data loggers used in this campaign is provided in Table 4.

Table 4. List of measurement equipment and specifications.

Type	Model	Manufacturer	Accuracy
Heat Flux Meter	HFP01	Hukseflux	±5% reading
NTC temp. sensor type N	FNA611	Ahlborn	±0.2 K
Data logger	Almemo 5690	Ahlborn	0.02% ± 2digits
Data logger	Almemo 2890-9	Ahlborn	0.02% ± 2digits
Pt100	FPA32L0100	Ahlborn	±0.3 K
Digital sensor for temperature, humidity, and pressure	FHAD 46/C2	Ahlborn	±2% RH, ±0.2 K, ±2.5 mbar

3.1.2 Drone-based External IRT Measurement Setup

The aerial survey of the building complex was carried out at night. This approach has significant advantages. Most relevant is the avoidance of solar radiation for the accuracy of the measurement. Furthermore, no or hardly any consideration has to be given to the operation of the building, and changes in the general conditions caused by users (changes in room temperature, window, and door openings) can be ignored.

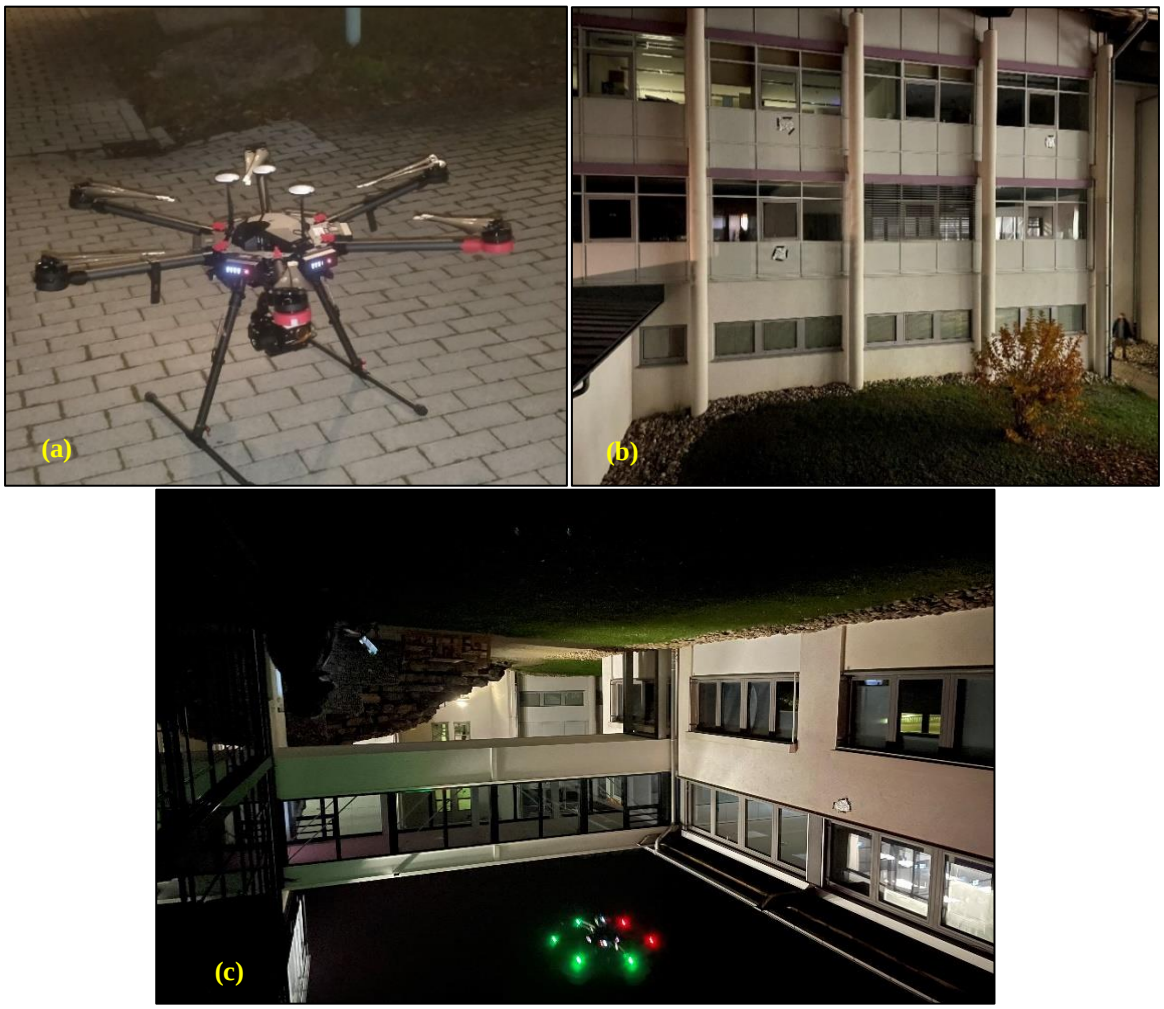

Figure 9. Setup for infrared thermography. (a) DJI Drone, (b) aluminum foils, (c) drone flight.

A system consisting of the DJI M600 Pro drone, the Gremsy S1 gimbal, and the Workswell Wiris Pro thermal camera [17] was used for the flight. A detailed description of the IR camera is given in Table 5.

Table 5. IR camera specifications.

Type	Property
Camera	IR camera
Model	WIRIS Pro
Manufacturer	Works well
Detector type	Uncooled VOx microbolometer
Wavelength	7.5 - 13.5 µm
Resolution	640×512
Measurement temperature	–40 - 550 °C
Working temperature	–10 - 50 °C
Accuracy	±2 K

The specified accuracy of ± 2K for IR cameras may appear too large for our application. However, it is important to note that this value takes into account multiple factors that need to be considered. The "Root-Sum-of-Squares" (RSS) technique used to determine the accuracy involves calculating partial errors for each variable in the temperature measurement equation, including emissivity, reflected ambient temperature, transmittance, atmosphere temperature, camera response, and calibrator (blackbody) temperature accuracy. By squaring the partial errors, adding them together, and taking the square root, the technique ensures that random errors do not add up in the same direction, which could lead to a larger deviation from the true value. However, it should be noted that the RSS analysis is only valid in the lab or at short ranges outside, as atmospheric absorption and emission can introduce uncertainty at longer ranges [48].

To validate the methodology, a measurement campaign was performed on a day when conditions were suitable. Before and during the IRT surveys, environmental variables including thermal radiation from the sky, wind speed, rain, sky conditions, and temperature gradient were observed. The building had not been exposed to snow or rain for 48 hours prior to the tests, and the sky was overcast for about 12 hours prior to and during the tests. Indoor air temperature was approximately constant before and during the test as all the offices were closed at night and outdoor temperature was also almost constant during the measurement. It should be noted that since the indoor temperature at various heights fluctuated due to natural convection (stack effect), the overall average indoor air temperature at the time of the survey was considered. Relative humidity and outside ambient temperature were measured with additional sensors. The average free stream wind speed during the day and then during the test were taken from the local weather station. The measurements were performed in the evening to early morning on an overcast night

(almost 2 hours after sunset) to minimize the effect of solar and night-sky radiation, and to minimize thermal mass effects.

Some challenges arose during practical implementation that also affected the analyzability of the data. The pre-planned flight routes, taking into account the recommended coverage rates (80-90%) [49], could not be flown automatically since wind conditions, GPS interference from metallic building structures and, in some places small distances between trees and façade would have meant too great a risk of collision. However, manual flight image acquisition had the consequence. Firstly, significantly less building area could be covered than planned. Secondly, a satisfactorily accurate correction of the drone's GPS position information was not possible with the currently available software products, either based on the thermal data or with the poorly exposed optical images taken in parallel. Taking into consideration the aforementioned factors, the subsequent section outlines the methodology employed for evaluating thermal images. The primary objective of this methodology is to determining the surface temperature, error reduction in the IR camera, and calculate the U-value of the building envelope.

3.2 Quantitative Image Evaluation

Figure 10 shows the overview of all governing equations that are required for the U-value estimation of the building envelope using drone-based infrared thermography. All the variables and their quantity are listed in Table 6. The following sections describe the methodology applied in this thesis for the possible infrared image texturing, analysis of thermal images, surface temperature measurement, blackbody correction for error reduction in infrared cameras and U-value estimation.

Table 6. List of variables used for calculating U-value.

Variable	**Quantity**
U	Thermal transmittance
T_{s}	Surface temperature
$h_{\mathrm{comb,out}}$	Combined heat transfer coefficient
$T_{\mathrm{air,out}}$	Outside air temperature
$T_{\mathrm{air,in}}$	Inside air temperature
v	Wind speed
τ_{atm}	Atmospheric coefficient
ε	emissivity
L_{obj}	Object radiance
L_{refl}	Reflected radiance
ρ	reflectivity
E_{i}	Incident irradiance
d	distance
T_{atm}	Atmospheric temperature
RH	Relative humidity
ΔL	Correction factor
$L_{\mathrm{BB}}\ (T_{\mathrm{S,ref,meas,IR}})$	Blackbody reference radiance with IR
$L_{\mathrm{BB}}\ (T_{\mathrm{S,ref,meas,NTC}})$	Blackbody reference radiance with NTC
$\varepsilon_{\mathrm{ref}}$	Reference blackbody emissivity
$P_{\mathrm{obj,wall}}$	Object wall position
P_{cam}	Camera position

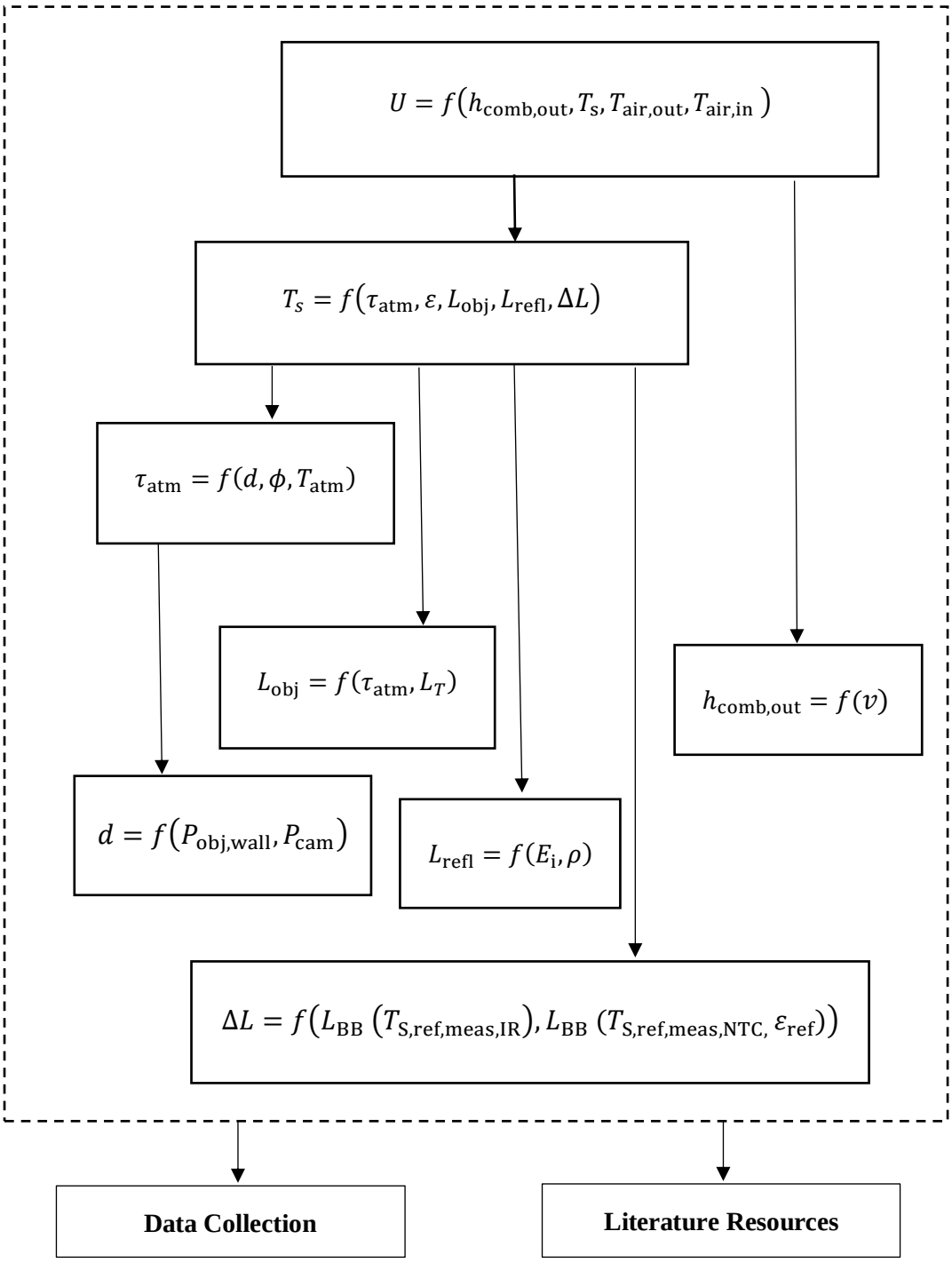

Figure 10. Governing functions to evaluate U-value in the flowchart.

3.2.1 Image texturing

Building Information Modeling (BIM) is a powerful tool for digitalizing processes in the construction and real estate industry. BIM can theoretically accompany all steps in the life cycle of a building from planning to demolition, but its usage is not yet universal, and BIM rates vary significantly across construction projects worldwide [50]. In addition, semantically enriched geometry, which forms the basis of every BIM model and without which no digital planning process is possible, is generally not systematically digitized in existing building stock [51]. Several scientific and commercial approaches have been developed to address this issue, including plan-based, photogrammetric, and laser scanning methods. These methods can generate 3D geometries and store them in the open data standard IFC, but the enrichment with metadata such as U-values of building components remains a challenging task, especially if automation is desired [52].

For the building complex investigated here, an IFC model was created before this thesis, it is shown in Figure 11. To prepare for an IRT aerial survey, the IFC model was co-arranged with a photogrammetric point cloud from a daytime aerial survey to ensure a common coordinate system. The externally visible surfaces were then extracted from the IFC model using a simplified geometric analysis based on the Python interface of IfcOpenShell [37].

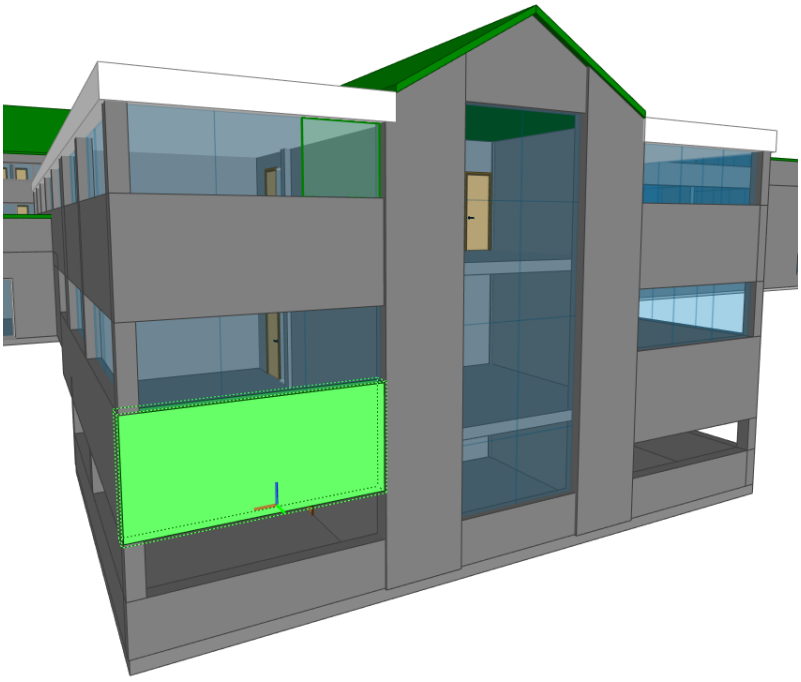

Figure 11. Part of the IFC 3D model

If the position and orientation of the camera (outer orientation), as well as the camera properties (inner orientation), are known with sufficient accuracy or calculated subsequently by photogrammetry software, objects with a likewise known position in the world can be retrieved on individual images using an algorithm prepared in this thesis according to this article [53]. In principle, this enables the texturing of exterior surfaces. Depending on the building structure and flight route, an algorithm should be used that avoids obscuring objects [54, 55], a feature that was not included in the software developed here.

3.2.2 Analysis of Thermal Images

The first step of the quantitative image evaluation is to analyze the thermal images taken with drone-based infrared thermographic measurement. The thermal images were imported and processed through the use of software called Workswell Thermolab version 0.9.0 in order to obtain the average temperature of surfaces which is necessary for this study. This software is supplied by the camera manufacturer and therefore contains camera-specific calculation algorithms. Therefore, areas of interest are identified and selected on the thermal image that is homogeneous in terms of material. A common example of selecting the areas to measure the average surface temperature is shown in Figure 12. Figure 12 shows the locations 1 and 2 wall areas which are homogeneous, and location 3 is the aluminum foil area for the reflected temperature measurement as described in the following section. Location 4 is where the radiometric info of the image can be changed as the software is able to do the atmospheric correction and the reflected temperature correction. Lastly, location 5, where minimun, maximum, and average temperature for the areas of interest can be seen.

Upon recording images, the camera-internal calibration parameters (emissivity, atmospheric temperature, distance, etc.) are used by the internal software to calculate temperature values. For these measurements, emissivity and distance were not pre-set in the camera to 100% and 0 m respectively, so atmospheric correction and reflected temperature correction was done by the software. In order to include the correction methodology in the thesis, restoration of the values was necessary. In Workswell's Thermolab software, this is only possible by adjusting single images as shown at location 4 in Figure 12. So, it was done for several example images, and a linear fit function was derived.

$$t_{100} = 0.9227789354979609\ (t_{95}) + 1.2104132389864246. \tag{22}$$

In the example data, no difference was observed between Thermolab's conversion for different images, and the linear fit matches the example data very well as shown in appendix A.4. After sating all the parameters, average temperature data was taken from the software. The following section describes the surface temperature measurements with the reflected temperature correction and the atmospheric correction.

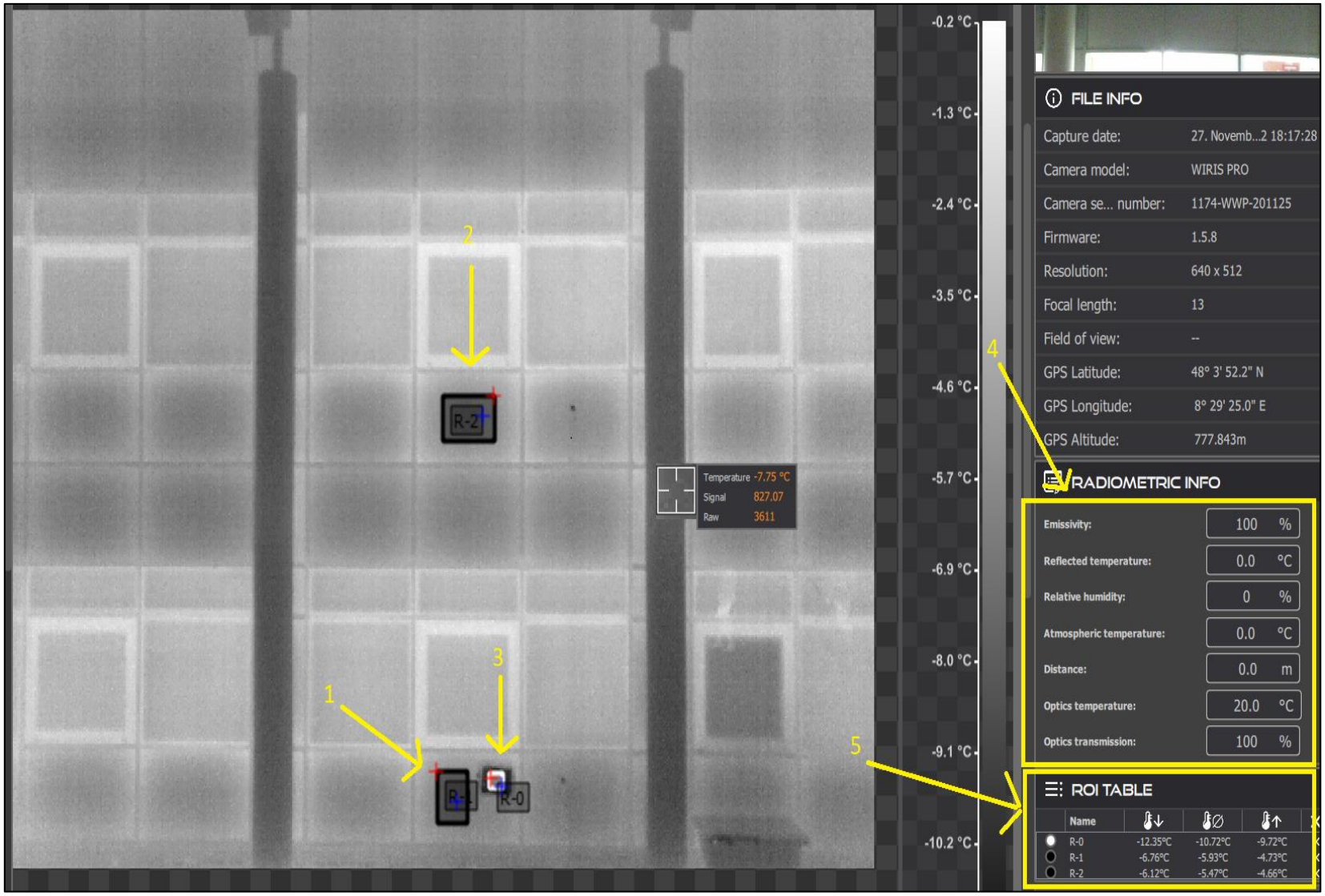

Figure 12. Thermolab software to evaluate surface temperature.

3.2.3 Surface Temperature Measurement

To obtain an accurate surface temperature measurement with an IR camera, accurate values of ambient air temperature, relative humidity, atmospheric transmittance, reflected apparent radiance, and emissivity should be determined during the post-processing of thermal images. The object emissivity for standard materials can be taken from the literature [21]. The way the ambient reflected radiation is measured depends on the type of application. In this work, the widely practiced aluminum foil method [22] is used for the ambient reflected radiation measurement.

Let us take a quick look at how the **aluminum foil method** works for measuring ambient reflected temperature. A detailed explanation of the method is described in ASTM E 1862-97 [22]. In this method, a crumpled and re-flattened aluminum foil is placed shiny side up on the wall surface as an infrared reflector. Then, the emissivity value of the visible foil area in the IR camera, needs to be set as 1.0. Afterward, the average temperature of that aluminum foil region is measured using an IR camera that gives us ambient reflected temperature and converted into ambient reflected radiance by integrating Planck's law (equation (3)) over the spectrum, weighted with the spectral response function [56]. The setup of aluminium foil on the wall surface (a) and IR image (b) is shown in Figure 13.

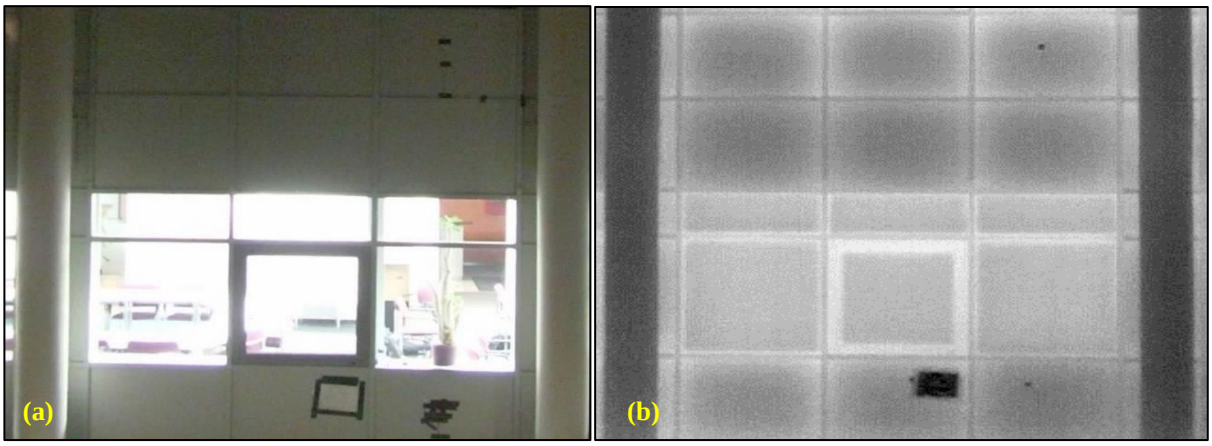

Figure 13. Aluminum foil setup for reflected temperature.

As described in the literature review, atmospheric transmission is an important parameter in infrared thermovision measurements [57]. Gas composition influences the results of measurements carried out by infrared thermography. Most important are absorbance coefficient: vapour absorbance α_{H_2O} and carbon dioxide absorbance α_{CO_2}. According to Gaussorgues [58] we have equation (23) for atmospheric coefficient,

$$\tau_{\mathrm{atm}} \cong \alpha_{\mathrm{H_2O}}. \quad (23)$$

The vapour absorbance depends on the number of absorbing molecules, i.e. on the partial pressure of water vapour, and the distance d travelled by radiation in the absorbing medium. It is usually accounted for by the height h of the cylinder with diameter D. There is a relationship between the height of the cylinder with water h, and temperature T_{atm}, relative humidity ϕ and distance d according to [58]. However, the atmosphere absorbs infrared energy differently depending on wavelength. For example, the atmosphere absorbs substantially all wavelengths between (5–7 μm). On the other hand, mid-wave (2–5 μm) and long-wave (8–14 μm) radiation is poorly absorbed by the atmosphere, allowing more infrared energy to reach the camera's sensor. Since the range of measured temperatures in this study was low (long-wavelength band), the absorption of long-wavelength radiation by IR camera is high considering the specifications of the camera [16]. Atmospheric temperature and relative humidity were measured during the measurement campaign. The distance between the camera and the object was calculated using the coordinate geometry of the image and camera position. A detailed explanation of all the relative equations can be found in [57]. Function (24) is used with the Passman and Larmore table to find the atmospheric coefficient.

$$h(T_{\mathrm{atm}}, d, \phi) = \left(1.6667 \cdot 10^{-4}\ {T_{\mathrm{atm}}}^3 + 10^{-2} \cdot {T_{\mathrm{atm}}}^2 + 0.38333\ T_{\mathrm{atm}} + 5\right) \phi \cdot d \cdot 10^{-4}, \quad (24)$$

where is h height of the cylinder with water in mm/km, T_{atm} is the ambient temperature in ° C, ϕ is relative humidity, and d is distance in km.

Considering distance d, the height of the cylinder with water h and wavelength γ, the appropriate values of $\alpha_{\mathrm{H_2O}}$ and $\alpha_{\mathrm{CO_2}}$can be determined using the Passman–Larmore tables. When these values are placed into equation (23), it is possible to calculate the atmospheric transmission coefficient τ_{atm}. The appropriate part of the Passman–Larmore tables is shown in appendix A.5 in Table 9 and Table 10.

In our case, all the infrared images were captured from a very close (< 10 m) distance, and also because of low absolute humidity and low temperatures that's why the transmissivity (τ_{atm}) is close to one ($\tau_{\mathrm{atm}} > 0.99$) and the emittance of the atmosphere part is very close to zero because of $(1 - \tau_{\mathrm{atm}})$ can be ignored, this parameter has little influence on the temperature measurement. On the other hand, the emissivity of the object and the reflected radiance have a very high influence on the temperature measurement and must be measured very accurately. After considering the assumption about the atmospheric transmissivity is close

to one, upwelled radiance from the atmosphere has very little influence on temperature measurement so equation (15) can be written as

$$L_{\text{tot}} = \tau_{\text{atm}} \varepsilon L_{\text{T}} + \tau_{\text{atm}} \frac{(1 - \varepsilon)}{\pi} E_{\text{i}}. \tag{25}$$

Therefore, the object's radiance at surface temperature can be calculated as

$$L_{\text{T}} = \frac{L_{\text{tot}} - \frac{(1-\varepsilon)}{\pi} \cdot E_{\text{i}} \tau_{\text{atm}}}{\varepsilon \, \tau_{\text{atm}}}. \tag{26}$$

Before calculating the surface temperature from the above equation, radiometric calibration and camera correction should be considered. First, let us talk about the radiometric calibration of atmospheric effects in the thermal and reflected regions of the spectrum. According to Schott [20], often the spectrally aggregated terms in the equation above are replaced with the equivalent values in the spectral band of interest by weighting by the sensor's normalized spectral response function $\beta(\lambda)$ which is provided by camera manufacturer [56].

$$L_{\text{T}} = \int L_{\text{T}\lambda} \, \beta(\lambda) \, \text{d}\lambda. \tag{27}$$

Furthermore, the integrated spectral bandpass values are frequently approximated as products of the integrated or averaged values. For instance

$$\int \varepsilon_\lambda L_{\text{T}\lambda} \tau_\lambda \approx \varepsilon_{\text{m}} L_{\text{T}} \tau_{\text{m}}, \tag{28}$$

"where ε_m is mean emissivity in the bandpass, τ_m is mean transmissivity to the sensor. As we know from our knowledge that equation (28) is not valid. It is, however, true to a good approximation if $L_{\text{T}\lambda}, \varepsilon_\lambda, \tau_\lambda$ are approximately constant over the spectral bandpass of interest, particularly if $\beta(\lambda)$ is approximately constant with λ" [20].

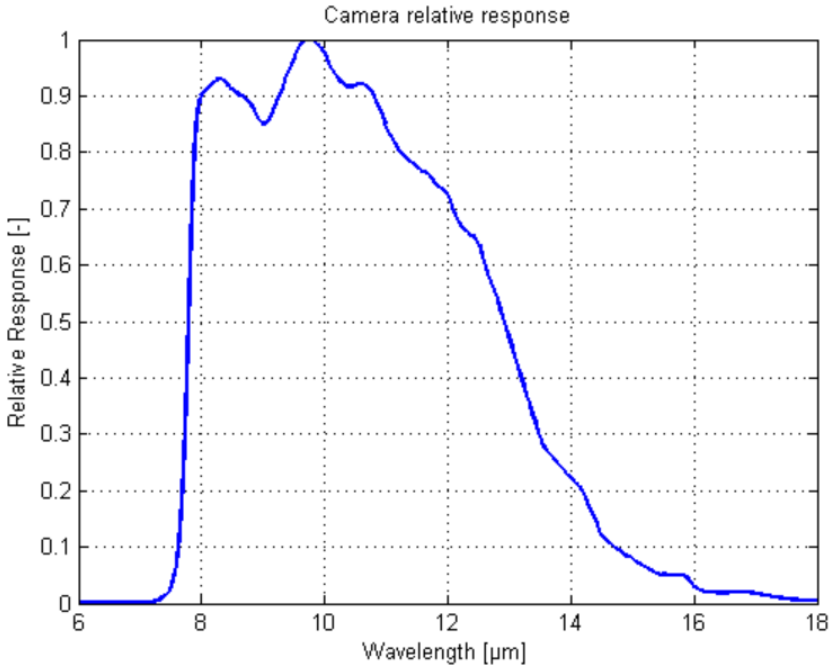

Figure 14. Spectral response function according to the wavelength [56].

Even if only one term varies with λ, equation (27) is a good approximation. From Figure 14 we can see, it is a good approximation to consider spectral response function as stated in equation (27) as $\beta(\lambda)$ is not constant with λ. In our calculation all the radiance values were interpolated with the camera's spectral response function.

Since the two most important quantities (surface temperature, and ambient reflected temperature) in the U-value analysis are measured using an IR camera, the error reduction in IR camera measurements is crucial in order to get accurate surface temperature and U-values. IR camera error reduction method is presented in the following section.

3.2.4 Error Reduction in Infrared Camera Measurement

To minimize inaccuracies in the camera itself, Non-Uniformity Correction (NUC) should be performed regularly. However, this does not avoid that the intrinsic radiation of the housing L_{cam} has a main influence on the recorded radiation in microbolometers [48, 59]. To avoid varying values due to changing camera body radiation, the camera manufacturer recommends an acclimatization time of 15 minutes [17]. In reality, absolute realistic values can only be achieved if a calibration is performed in the field during the measurement campaign. One common method to address this challenge is blackbody correction [37].

Blackbody Correction

A blackbody is a theoretical object that absorbs all incident radiation and emits radiation at the maximum possible rate for a given temperature. A practical implementation of a blackbody is to use approximately blackbodies treated with a varnish of known emission properties and to measure their surface temperature continuously. Ideally, these bodies should represent the upper and lower limits of expected radiation values of the measured objects [60]. This ensures that temperature is as accurate as possible and can be relied upon for critical applications.

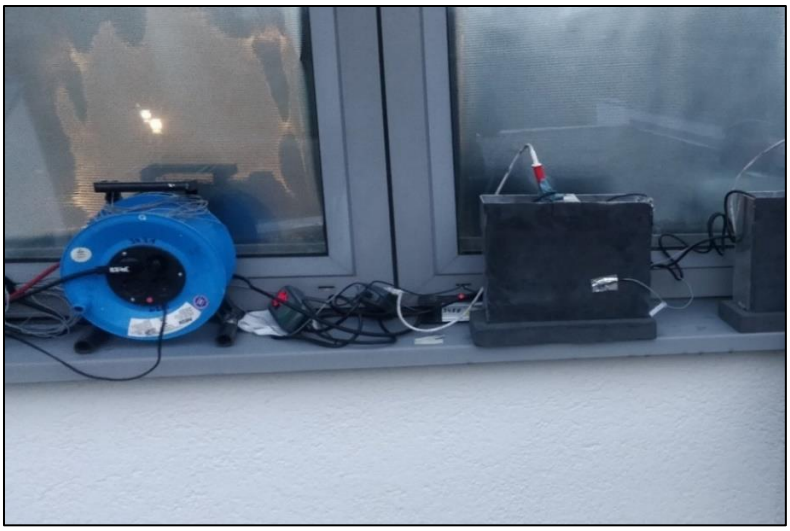

Figure 15. Reference body with temperature control and surface temperature measurement.

As shown in Figure 15, a closed aluminum bucket kind of structure is used with a thickness of 1.5 mm. Water is filled inside the empty space which acts as a heat capacitor medium to keep the blackbody temperature stable. In order to keep the water at the desired temperature throughout the measurement period, a temperature control unit is attached to the immersion heater, which is submerged in water. The outer surface that we used was first sand blasted to get a rough surface and then high emissivity paint is sprayed

on the surface. The black spray has an emissivity of 0.97 [61]. To compare the reading with the IR camera measurements, a reference NTC surface temperature sensor is installed. For mounting the surface temperature sensors, the reflective tape was used [27] to avoid ambient radiation effects. Most importantly, two blackbodies are used, one is kept at a higher temperature (20° C) using the submerged heater, and the other one is kept at 5° C. Both blackbodies are the same except for their water temperature. This provides, two reference temperatures to correct the IR camera measurements.

Based on equation (9), assumed that deviations result from an inaccurate internal correction for L_{cam}. Neglecting the atmospheric influence as $\tau_{atm} > 0.99$, below equations can be obtained,

$$L_{\mathrm{cam,old}} + L_{\mathrm{BB}}\left(T_{\mathrm{S,ref,meas,IR}}\right) = L_{\mathrm{obj}}(T_{\mathrm{S,ref,meas,NTC}}) + L_r + L_{\mathrm{cam,new}} \tag{29}$$

$$= \varepsilon_{\mathrm{ref}} \cdot L_{\mathrm{BB}}\left(T_{\mathrm{S,ref,meas,NTC}}\right) + \rho_{\mathrm{ref}} \cdot L_{\mathrm{BB}}\left(T_r\right) + L_{\mathrm{cam,new}}$$

and from this for the correction value

$$\Delta L_{\mathrm{cam}} = L_{\mathrm{cam,new}} - L_{\mathrm{cam,old}} \tag{30}$$

$$= L_{\mathrm{BB}}\left(T_{\mathrm{S,ref,meas,IR}}\right) - \varepsilon_{\mathrm{ref}} \cdot L_{\mathrm{BB}}\left(T_{\mathrm{S,ref,meas,NTC}}\right) - (1 - \varepsilon_{\mathrm{ref}})\, L_{\mathrm{BB}}\left(T_r\right)$$

taking into account the temperature $T_{\mathrm{S,ref,meas,IR}}$ originally output by the thermal camera as the measured value for the reference body temperature, the surface temperature $T_{\mathrm{S,ref,meas,NTC}}$ measured on the reference body with NTC sensor, the emissivity $\varepsilon_{\mathrm{ref}}$ and reflectivity ρ_{ref} of the paint available as spectral values [61], and an estimated ambient radiation temperature of the environment T_{r}. This approach is based on the assumption that the influence of the housing temperature remains approximately constant after the acclimatization period with the continuous operation (the camera was turned off only for a few seconds during the battery change of the drone) and approximately constant ambient conditions. To sum up this section, an error reduction approach is developed using blackbody for the two most important parameters: surface temperature and reflected ambient temperature measured by an IR camera. Using this correction approach, a large deviation of the IR camera error is brought under control, which can be seen in the result section. The following section describes the U-value measurement after correcting the surface temperature.

3.2.5 U-value Measurement

The overall thermal transmittance of the wall was estimated by assuming that the heat flow is passing through the elements, and transferred to the IR camera sensors through radiation. In order to accurately calculate the radiated heat flow, it is necessary to consider the view factor of all nearby objects as well as their temperatures in the field of vision of the wall assembly under study. The view factor is the degree to which heat carried by radiation can be passed between two surfaces.

Since the measurement campaign in this study is performed on overcast skies and the ambient air temperature was stable several hours prior to the tests, it was approximated that temperatures of the sky, the ground, and surrounding objects are in thermal equilibrium with ambient air. Therefore, the radiation heat exchange of surfaces was assumed to be with the ambient air, and the view factor is equal to 1 [62].

In this study, the instantaneous U-value was calculated using Equation presented by Dall'O et al. [42]

$$U = q_{\mathrm{rad}} + q_{\mathrm{cv}} = h_{\mathrm{comb,out}} \left(\frac{T_{\mathrm{s}} - T_{\mathrm{air,out}}}{T_{\mathrm{air,in}} - T_{\mathrm{air,out}}} \right), \tag{31}$$

where T_s is the external surface temperature of the façade, $T_{\mathrm{air,in}}$ is the indoor air temperature, $T_{\mathrm{air,out}}$ is the outdoor air temperature, and $h_{\mathrm{comb,out}}$ is the combined (i.e. including radiation and convection) heat transfer coefficient.

The influence of the heat transfer coefficient can be observed from equation (31), with its value directly affecting the U-value. In the standard calculations of the external heat transfer coefficient, pre-calculated values or simple equations are provided by the technical standards, such as ISO 6946-1 [13]. In this thesis, the air speed parameter was determined by selecting the air velocity from the data of the nearest weather station. Due to the lack of available data from the installed weather station on site, the data from the nearest weather station was used instead. This allowed for a more analytical evaluation of the external heat transfer coefficient $h_{\mathrm{comb,out}}$.

Calculation of Convective Coefficient: Two methodologies were employed to calculate the convective coefficient based on actual weather conditions observed during the survey. The first method involves using the Jurges equation [43], which is a simplified approach considering both convection and radiation losses.

This dimensional equation accounts for the average surface wind speed and its direction, ensuring a comprehensive assessment of the convective heat transfer coefficient h_c

$$h_c = 5.8 + 3.8054\, v \ (v < 5 \text{ m/s}), \tag{32}$$

where, v is wind velocity near the building element. According to Palyvos [63], many uncertainties still exist in this field. Ongoing additional studies are currently being conducted on a full-scale experimental building to further enhance the accuracy of measuring the convective heat transfer coefficient for the U-value assessment of external walls at the site.

For comparative analysis, a more complex methodology was explored, which involves the separate calculation of radiation and pure convection contributions. Similar to the Jurges equation, this method incorporates variables such as wind speed, air temperature, and surface temperature. Both equations are derived from the ASTM C 680 standard, serving as the reference source [43].

So, the contribution due to pure convection is calculated using,

$$h_{cv} = 15.89 \left(\frac{1}{600}\right)^{0.2} \left(\frac{1}{T_s}\right)^{0.181} \left(\left(T_s - T_{air,out}\right)^{0.266}\right) \sqrt{1 + 0.7935\, v}. \tag{33}$$

The calculation of the convective coefficient's radiation component involves the utilization of the following equation

$$h_{rad} = \frac{5.67 \times 10^{-8}\, \varepsilon \left({T_s}^4 - {T_{air,out}}^4\right)}{\left(T_s - T_{air,out}\right)}. \tag{34}$$

The values of the convective coefficient calculated by the two methods are comparable for a wind speed of less than 2 m/s. Therefore, in order to simplify the calculation methodology, Jurges equation was used that depends only on the wind speed as during the measurement campaign wind speed was approximately under 2 m/s. [42] Expecting satisfactory results from this overall method is a big question because the local weather station is too far from the measurement site and also Jurge's model is based on approximation. After considering all the boundary conditions, this is the best that is applicable here and used to showcase the overall method.

4 Results and Discussion

This chapter presents the results obtained after applying the methodology to analyze thermal images for the final U-value measurement. The first part of the chapter presents the possible image texturing on infrared images. The second section presents the outcome of the analysis of thermal images without any correction and emphasizes the importance of camera calibration for accurate surface temperature measurement. The third section evaluates the correction factor using the reference blackbody correction method. In the fourth section, surface temperature results after correction are presented for two example façades. Finally, the fifth section calculates the U-value using the drone-based infrared thermography method and compares with the reference U-values obtained through the HFM method.

4.1 Image Texturing

This section discusses the results of possible infrared image texturing. Due to the challenges stated in the methodology section 3.1.2, a satisfactorily accurate correction of the drone's GPS position information was not possible with the currently available software product, which resulted in false image texturing as shown in Figure 16. Figure 16 shows two triangles, where the red triangle represents the surface area extracted from BIM and the black triangle is a result after applying the algorithm for the image texturing described in section 3.2.1.

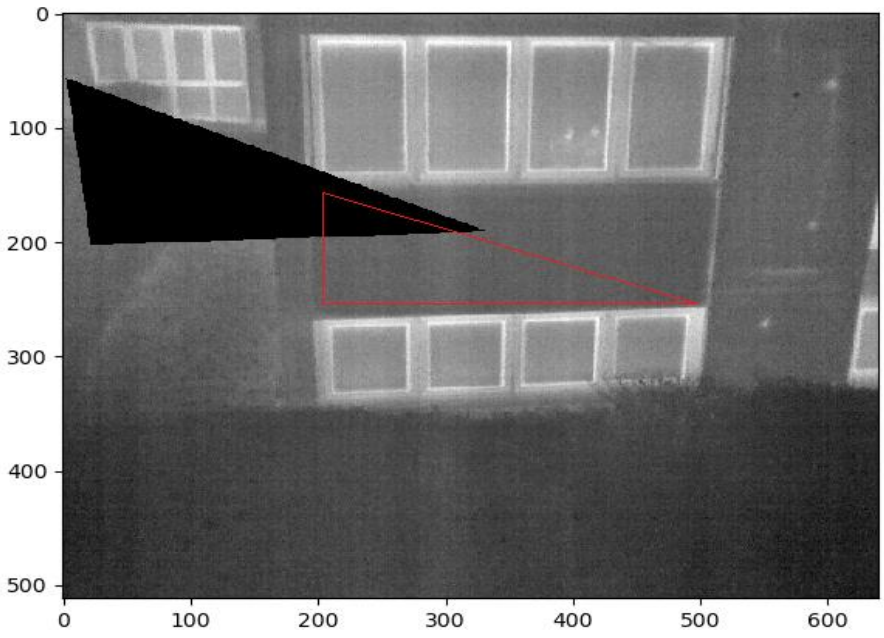

Figure 16. Triangle detection in infrared image for image texturing.

To achieve accurate retrieval of objects in individual images, it is necessary to have precise knowledge of the camera's position, orientation, and properties. This information can either be known with sufficient accuracy or calculated subsequently using photogrammetry software. Once these parameters are established, objects with known positions in the real world can be accurately retrieved in the images. This capability allows for effective texturing of exterior surfaces. Since an automated solution for image positioning and automatic texture extraction is not currently available, a manual evaluation of individual images was performed to obtain the results presented in the following section. This approach ensures the accuracy and reliability of the evaluation process, considering the specific complexities of the images and the limitations of existing automated methods.

4.2 Raw Thermal Image Analysis

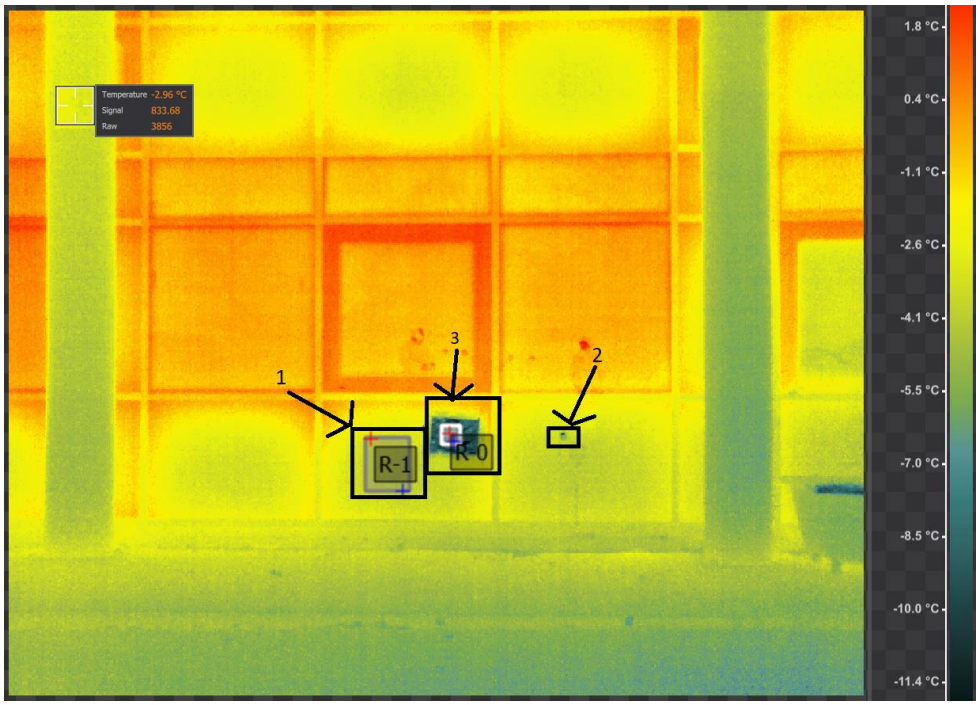

Figure 17. IR image of an example façade taken by drone-based IRT. (1) Surface temperature measured area, (2) HFM sensor, (3) Reflected ambient temperature measured area using aluminium foil.

This section discusses the analysis of raw thermal images captured by drone-based infrared thermography. The images were captured during the measurement campaign described in section 3.1.2. The objective of this analysis was to compare the surface temperature measurements obtained from the drone-based system with the reference NTC surface temperature measurements. The analysis revealed significant deviations between the two measurements, indicating the presence of measurement errors. An example of the analysis conducted on a façade is presented in Figure 17, where location 1 shows the region of interest for the surface temperature, and location 2 shows the NTC sensor. At the time of measurement, the surface temperature measured with the NTC sensor was 3.6 °C, while the measurement with the drone-based infrared camera for the region of interest was –3.5 °C.

To ensure the reliability of the results, various image analyses were carried out at different times, and similar trends were observed. These findings suggest that the measured object temperature is affected by the IR camera body temperature and convective cooling effects induced by the drone propellers on the camera. This is consistent with the observations made in another study [64], which reported that the ambient temperature around the camera has a significant impact on the calibration of radiometric thermal cameras by altering the camera body temperature.

However, even in the grounded experiment, the surface temperature deviated significantly, indicating that the IR camera may not be calibrated or that external environmental conditions may affect its performance to a greater extent. As the IR camera was calibrated before the measurement campaign, and yet it showed a considerable measurement error, a recalibration approach was used to correct the deviation. This correction was performed using a known blackbody during the measurement campaign, as explained in section 3.2.4. The blackbody provided a known reference temperature, allowing for the calibration of the IR camera. The following section presents the results of the camera calibration using the reference blackbody.

4.3 Reference Blackbody Correction

The measurement of U-values using an IR camera is susceptible to errors caused by the non-uniform response of the camera. Since small deviations in surface temperature can lead to significant errors in U-value calculations, the accuracy of the IR camera measurements is crucial. The testing of the IR camera during the measurement campaign revealed noticeable errors in its measurements. Therefore, it is beneficial to perform blackbody correction during the measurement campaign to improve the accuracy of temperature measurements. This section aims to evaluate the effectiveness of the blackbody correction method, as described in section 3.2.4, for correcting temperature measurements using from IR camera.

To evaluate the effectiveness of the blackbody correction method, a series of measurements were conducted on reference bodies using drone-based infrared thermography, as described in section 3.1.2, at three different times during the night: 19:40, 1:52, and 4:24. Multiple images were taken during each flight time, and the reference bodies' temperatures were measured using NTC sensors throughout the measurement campaign. Equation (30) was used to obtain the time course of ΔL_{cam} by comparing the NTC-measured surface temperatures with the recorded radiation values from the IR camera. The mean values of the three measurement times were used to obtain ΔL_{cam}.

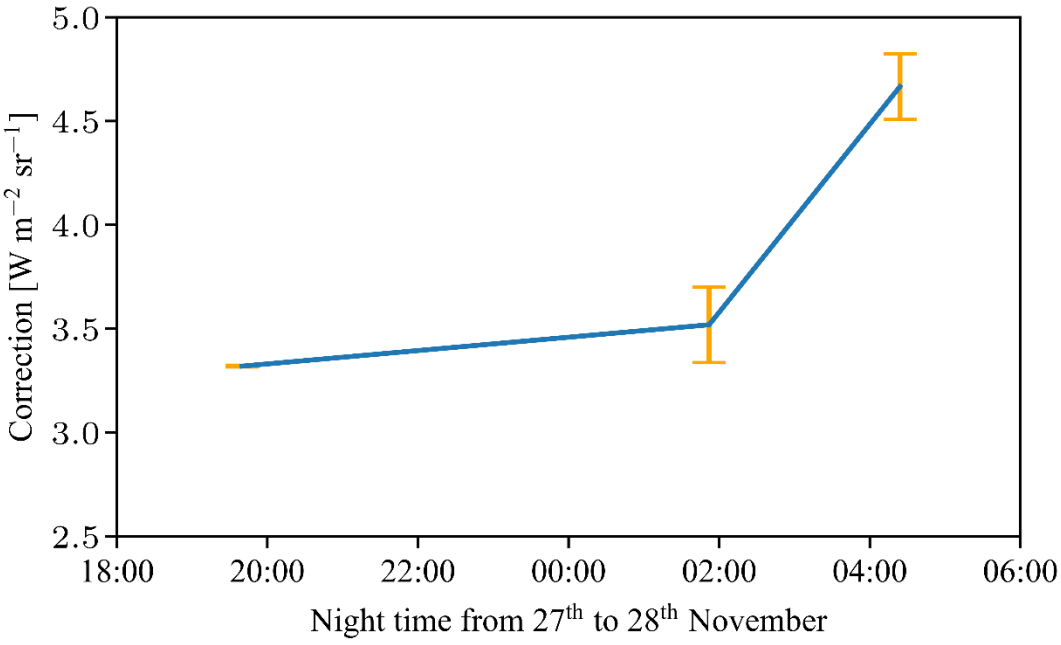

Figure 18. Time course of the correction value ΔL_{cam} from three measurement times with standard deviation of the repeat measurements at the same measurement time.

Figure 18 shows that the error in the IR camera is not constant throughout the measurement period. The values interpolated over time were used to correct the infrared images on the façades to calculate accurate surface temperatures in the following sections. The scatter shown in Figure 18 indicates a significant uncertainty in the determination of ΔL_{cam}. Therefore, the assumption of an approximately constant influence of the housing temperature from section 2.2 must be questioned.

In this result section, a reference blackbody error reduction approach is utilized for IR camera correction. However, it is observed during data analysis that the IR camera body temperature has an impact on the object temperature measurement. The camera calibration approach used in this study had weaknesses in practical application due to the fluctuating accuracy of the camera under different ambient temperatures during flight. To address this issue, reference values such as contact temperature sensors on every investigated surface may be necessary for almost every image, but this would increase data acquisition effort and partially negate the advantages of the system. However, such an approach could provide an advantage in determining local emissivity. Future research should focus on exploring hardware-level solutions to improve camera accuracy and alternative calibration approaches that balance accuracy and data acquisition effort.

4.4 Surface Temperature of the Façade

4.4.1 A-North Façade

Figure 17 presents an IR image of the north façade captured by the Workswell Wiris Pro thermal camera. Contact surface temperature sensors and aluminum foil are mounted at locations 2 and 3 respectively. The square region under the window (location 1) is the region of interest for the IRT measurement. In Figure 8 (a), the outer wall surface of the A-North façade is visible. At the same wall location, but on the inside wall surface, two HFM sensors, surface temperature sensors, and air temperature sensors are also mounted as described in section 3.1.1. The whole setup is used to calculate the reference U-value of the wall element. The reference HFM U-value result is presented in section 4.5.1.

A series of measurements were conducted on the A-north façade with the drone-based infrared thermography as described in section 3.1.2 at 18:18, 18:25, 1:05, and 1:36. Figure 19 shows a comparison of the surface temperature of an element of the A-North façade of the building complex determined with an NTC contact sensor and the thermographic method presented. The error bars of the thermographic temperature values only illustrate the influence of the ΔL_{cam} scattering (see Figure 18).

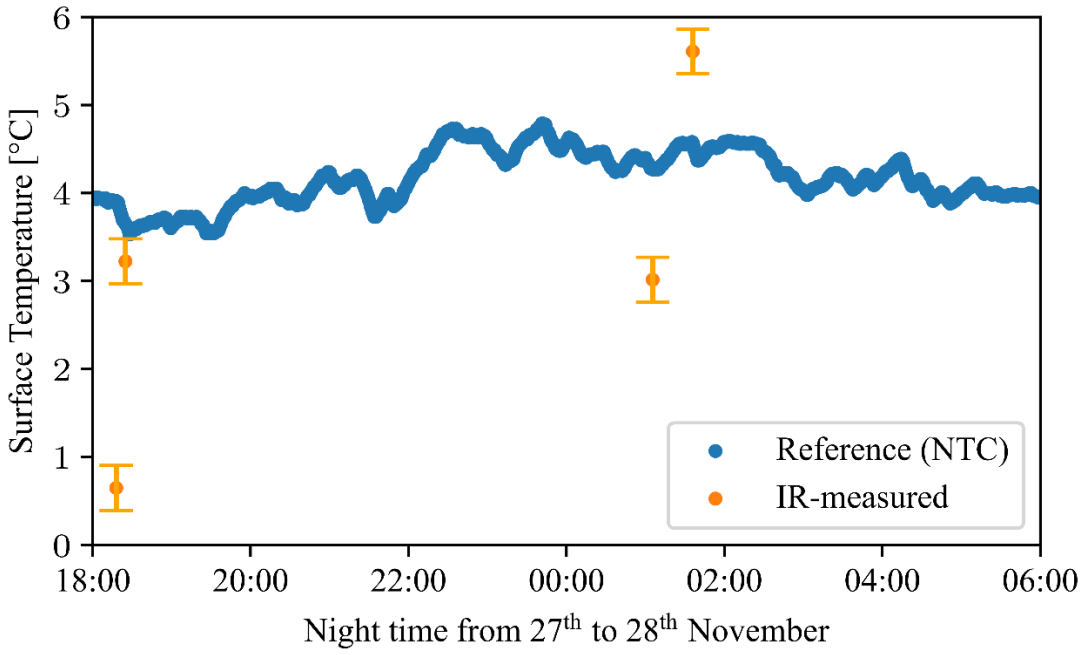

Figure 19. Comparison between surface temperatures measured by thermography and by NTC contact thermometer on a A-North façade. The error bars refer to the effect of the overlapping standard deviation of ΔL_{cam} from Figure 18.

As illustrated in Figure 19, at 18:18, the IR camera recorded an average surface temperature of 0.648 °C, while the reference NTC temperature measurement yielded 3.91 °C. At 18:25, the IR camera and the reference NTC sensor recorded average surface temperatures of 3.22 °C and 3.61 °C, respectively. It is worth noting that the drone flight measurement campaign began at 18:14. The difference between the IR camera measured and NTC measured temperature was –3.262 °C and –0.39 °C at 18:18 and 18:25 respectively. It is clearly visible from the large deviation at 18:18 that the IR camera requires time to warm up and it exhibits a large error during early flight time because its body temperature drops while on standby mode. As stated in the methodology section, small errors in temperature measurement can lead to significant errors in the U-value. Therefore, the early flight images were excluded from U-value calculations during the data analysis of infrared images.

At 1:05, the average surface temperature was measured using an IR camera and a reference NTC temperature sensor, yielding values of 3.01 °C and 4.28 °C, respectively. At 1:36, the IR camera and NTC sensor measured average surface temperatures of 5.69 °C and 4.58 °C, respectively. The difference between the IR camera and NTC measurements was –1.27 °C and 1.11 °C at 1:05 and 1:36, respectively. The early flight images were excluded from the analysis, resulting in an error range of –1.27 to 1.11. This range is well within the reported accuracy of the IR camera (±2 K). For the application of U-values measurement, it should be far lower here because the majority of uncertainties are controlled while measuring the surface temperature as explained in section 3.1.2.

4.4.2 D-South Façade

Figure 20 displays the captured IR image of the D-South façade using the Workswell Wiris Pro thermal camera. Location 1 is where the aluminum foil is mounted, while location 2 has contact surface temperature sensors. The region of interest for the IRT measurement is the large square area under the window, denoted as location 3. In Figure 8 (d), the outer wall surface of the D-South façade is visible. Additionally, at the same wall location, but on the inside wall surface, two HFM sensors, surface temperature sensors, and an air temperature sensor are installed as described in section 3.1.1. This entire setup enables the calculation of the wall element's reference U-value. The reference HFM U-value result is presented in section 4.5.1.

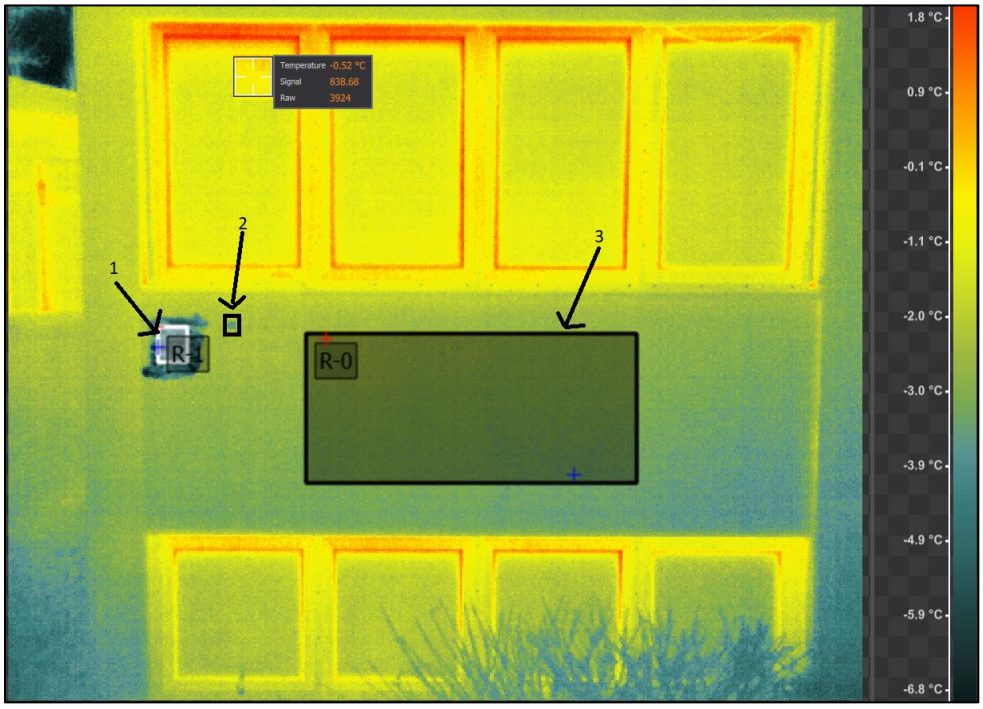

Figure 20. Thermolab analysis image for D-South façade.

Measurement of the D-South façade using drone-based infrared thermography was conducted at multiple time points: 19:08, 22:50, 22:58, and 4:07, as described in section 3.1.2. Figure 21 presents a comparison between the surface temperature of an element on the south façade of the building complex obtained using the NTC contact method and the presented thermographic method. The error bars associated with the thermographic temperature values represent the impact of the ΔL_{cam} scattering, as shown in Figure 18.

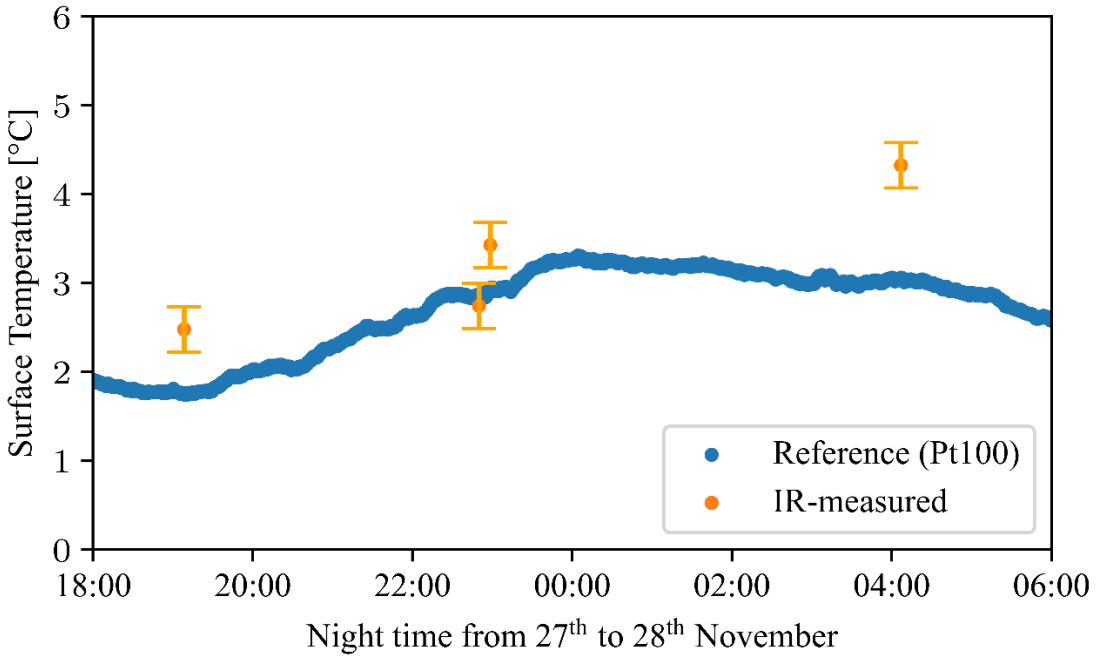

Figure 21. Comparison between surface temperatures measured by thermography and by Pt100 contact thermometer on a D-South façade. The error bars refer to the effect of the overlapping standard deviation of ΔL_{cam} from Figure 18.

Figure 21 illustrates the comparison of average surface temperatures measured at different time points. At 19:08, the IR camera measured an average temperature of 2.478 °C, while the reference Pt100 temperature was 1.76 °C. At 22:50, the IR camera recorded an average temperature of 2.72 °C, while the Pt100 measurement was 2.87 °C. During the same flight at 22:58, the IR camera measured an average temperature of 3.43 °C, while the Pt100 measurement was 2.93 °C. The sudden temperature change could be due to differences in the distances from which the images were taken. To avoid this issue, a measurement campaign using the autopilot was planned for our study but was not possible due to difficulties mentioned in section 3.1.2. At the end at 4:07, the average surface temperature measured with the IR camera was 4.32 °C, while the measurement with reference Pt100 temperature was 3.05 °C. The deviation range between the IR camera and Pt100 sensor measurements was found to be between – 0.15 and 1.27. However, this range is within the reported accuracy of the IR camera (±2 K).

The section described the measurements conducted on the north and south facades of the building using drone-based infrared thermography. The IR images of both façades were captured using a Workswell Wiris Pro thermal camera, and contact surface temperature sensors and aluminum foil were mounted at specific locations for the reference U-value calculation. The thermographic method was compared with NTC and Pt100 contact thermometers on A-north and D-south façades respectively to obtain the surface temperature

of the facades. The results showed that the IR camera requires time to warm up and exhibits large errors during the early flight time. Therefore, early flight images were excluded from the U-value calculations. The error range obtained from the IR camera was well within the reported accuracy (±2 K) of the camera. The section also includes figures of the IR images and the comparison between the thermographic and reference measurements.

4.5 U-value calculation

This section covers the results of the U-value measurement using HFM and IRT methods. First, section 4.5.1 presents the U-value calculation using the HFM method according to ISO 9869-1 average method. Then, the U-value estimation using drone-based infrared thermography is presented in section 4.5.2. drone-based infrared thermography results are based on surface temperatures measured over the course of the night as presented in section 4.4.

4.5.1 Heat Flux Meter Result

This section aimed to estimate the U-values of selected façades (A-North, D-South, and E-South) of an exemplary building using the ISO 9869-1 average method [27]. The building and its blocks detail were described in detail in section 3.1 and the complementary floor plans with detailed locations can be found in the appendix A.1, A.2, and A.3. The U-values were also estimated using a look-up table based on the building age as a comparison of this method.

The ISO 9869-1 average method involved the use of heat flow and temperature sensors to measure the U-value of each façade. The collected data were filtered to comply with the standard and only readings taken from sunset to sunrise were used to avoid the effects of solar radiation. Equation (19) was used to calculate the HFM U-value for all façades, which were monitored for over 72 hours in November. During this period, indoor and outdoor surface temperatures and heat flow rates were recorded at 30-second intervals as shown in Figure 22 and Figure 23. During the data analysis, data were filtered according to the method described in section 0. The inside surface temperature range for the A-North façade fluctuated between 14.2 °C to 18.0 °C, the outside surface temperature ranged from –3.36 °C to 6.88 °C, and the heat flux rate oscillated between 15.1 to 31.1 W/m^2. Similar analyses were performed for the other two façades.

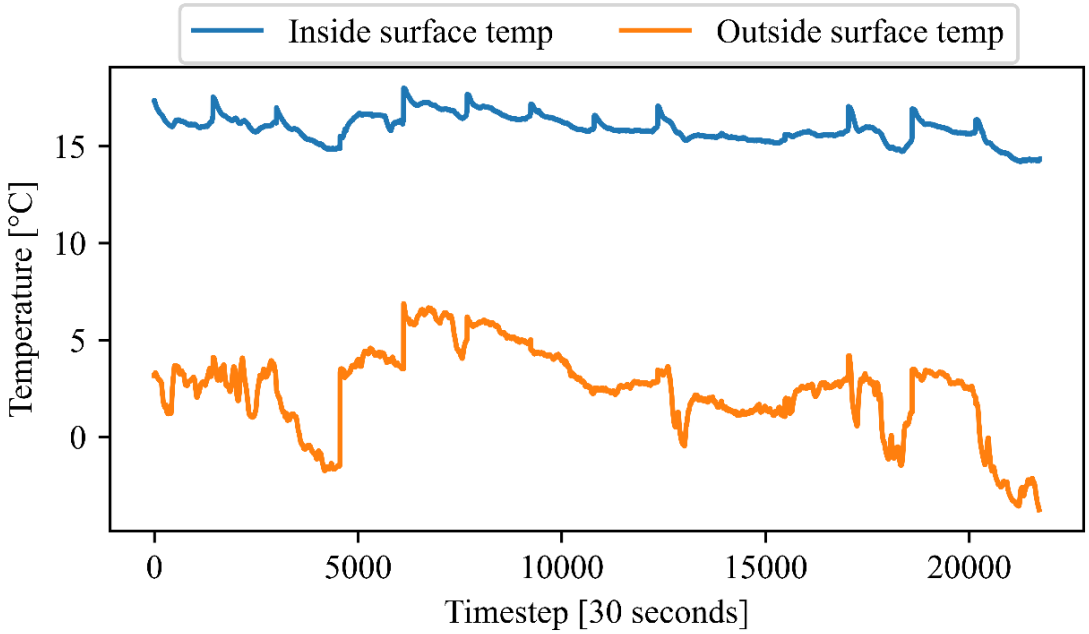

Figure 22. Measured inside and outside surface temperature at a A-north façade (after filtering sunrise to sunset time)

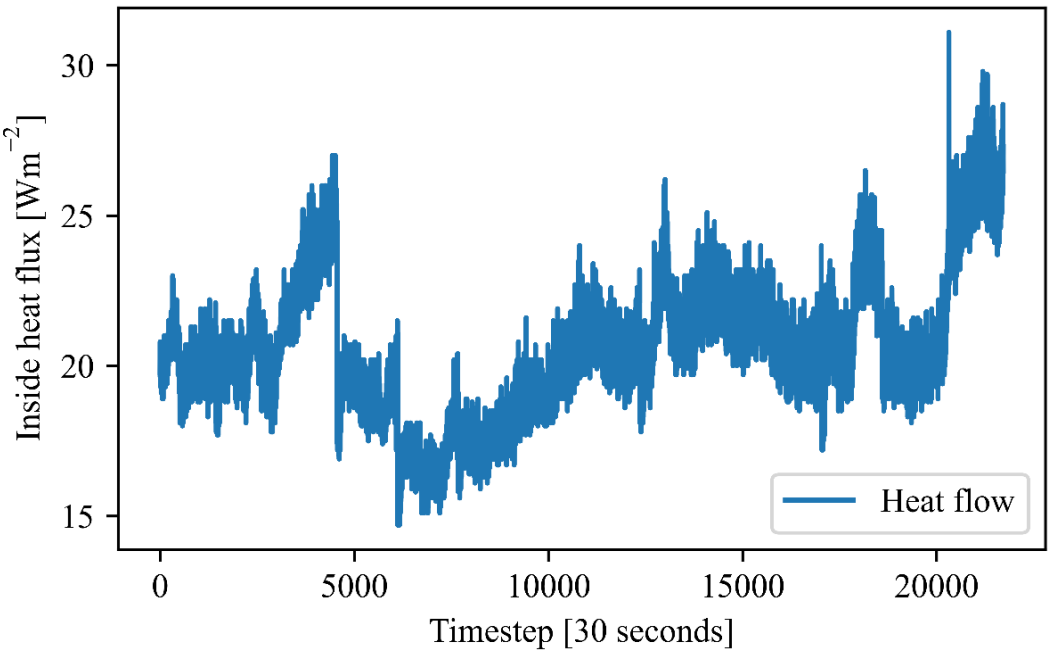

Figure 23. Measured heat flow at a A-north façade (after filtering sunrise to sunset time).

The results showed that the typical U-values for each façade, based on the building age, were 0.85 W/m^{2}K for the A-North façade, 0.35 W/m^{2}K for the D-South façade, and 0.2 W/m^{2}K for the E-South façade [65].

The U-values estimated using the ISO 9869-1 average method were found to be 1.21 ± 0.17 W/m^{2}K for the A-North façade, 0.58 ± 0.08 W/m^{2}K for the D-South façade, and 0.20 ± 0.03 W/m^{2}K for the E-South façade. The results are summarized in Table 7.

Table 7. Typical U-value (GEMOD) and HFM measured U-value using the average method.

Block-Façade	**Age**	**Duration (Date)**	**HFM measured U-value (W/m^{2}K)**	**Typical (GEMOD) U-value (W/m^{2}K)**
A-North	1989	14.11. to 24.11.	1.21 ± 0.17	0.85
D-South	1998	24.11. to 08.12.	0.58 ± 0.08	0.35
E-South	2019	14.11. to 24.11.	0.20 ± 0.03	0.15

The results indicate that the estimated U-values for the selected façades using the ISO 9869-1 average method are significantly higher than the typical values based on the building age. This discrepancy may be due to factors such as the presence of moisture and aging, which were not considered in the typical U-values. The results also demonstrate the effectiveness of the ISO 9869-1 average method in estimating U-values of building façades. The HFM-measured U-value results have been utilized as a reference value for evaluating the accuracy of drone-based infrared thermography results. This comparison is discussed in detail in the subsequent section.

4.5.2 Drone-based Infrared Thermography Results

This section aims to estimate the U-values of selected façades (A-north, D-south, and E-south) of an exemplary building using the drone-based infrared thermography as described in section 3.2.4. The parameters measured by the IR camera were corrected using blackbody correction, and the U-value was calculated using the corrected parameters. The measurement campaign was conducted during the month of November. The U-values estimated using the IRT method and the HFM method were compared and the percentage deviation between the two methods was calculated. The resulting U-value for all façades is presented in Table 8 along with the reference U-value calculated using the average HFM method.

Table 8. U-value of the façades with IRT and HFM.

Block-Façade	**U-value (W/m^2K) with IRT**	**U-value (W/m^2K) with HFM**	**U-value Deviation (%)**
A-North	1.04	1.21	16.34
D-South	0.73	0.58	20.54
E-South	0.37	0.20	45.94

The U-values estimated using the IRT method for Façade A-North, D-South, and E-South were 1.04 W/m^2K, 0.73 W/m^2K, and 0.37 W/m^2K respectively. In comparison, the U-values obtained using the HFM method for Façade A-North, D-South, and E-South were 1.21 W/m^2K, 0.58 W/m^2K, and 0.20 W/m^2K respectively. The percentage deviation between the two methods for Façade A-North, D-South, and E-South were 16.34%, 20.54%, and 45.94% respectively.

Discussion

Although the results seem reasonably accurate here, the previous section shows that some uncertainties need to be reduced to reach an accurate measurement. There were some variations between the U-values estimated using the IRT and HFM methods, particularly for façade E-South. The higher percentage deviation for façade E-South can be attributed to the uncertainties associated with the IRT method, such as errors in camera calibration, the emissivity of the surface, atmospheric conditions, the geometry of the wall, and wind speed. The HFM method provides a direct measurement of the heat flux through the wall, whereas the IRT method estimates the U-value indirectly by measuring the surface temperatures of the wall and assuming certain boundary conditions.

The accuracy of wind speed estimation is crucial for U-value calculation because any error in wind speed estimation can lead to inaccuracies in the U-value calculation. Wind speed affects the convective component of the U-value, which is calculated according to the equation (32). U-value is directly proportional to the convective coefficient and the convective coefficient is directly proportional to the wind speed. Wind speed plays a significant role in the overall heat transfer rate through the building envelope as shown in Figure 24. The thickness of the boundary layer and its convective heat transfer coefficient depends on the wind speed, and hence an accurate measurement of wind speed is necessary for the accurate calculation of the U-value.

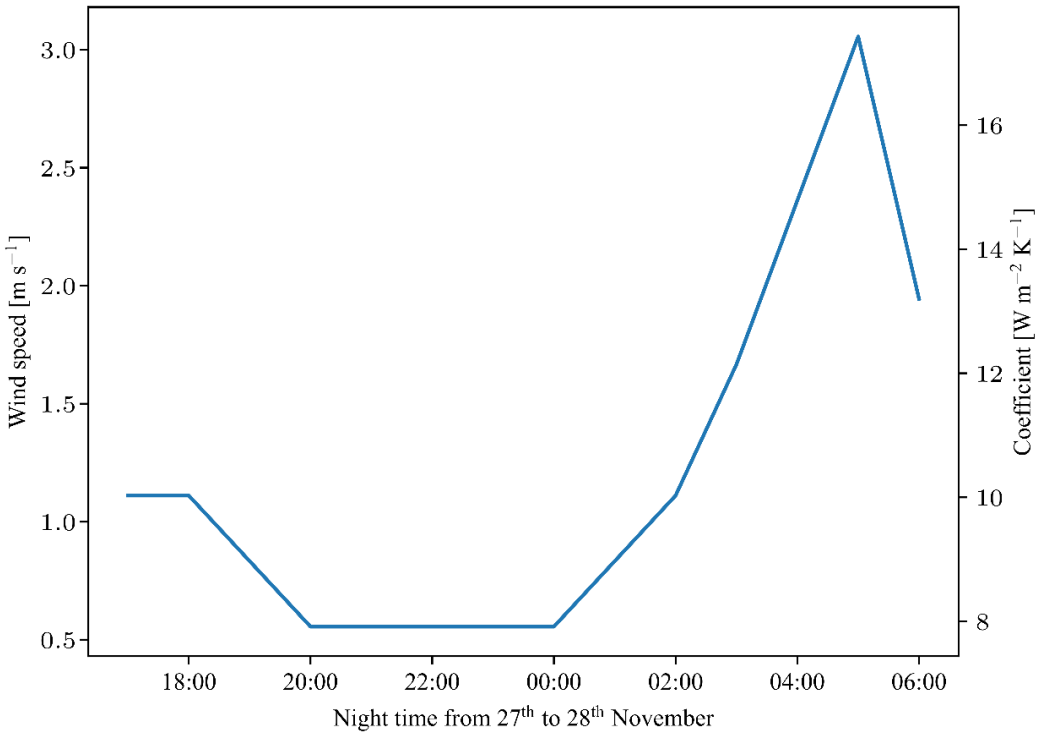

Figure 24. External convective heat transfer coefficient calculated using equation (32).

Inaccuracies in wind speed estimation can occur when wind data is taken from nearby weather stations, as the wind speed can vary significantly from location to location due to factors such as local topography and building orientation. It is important to consider the effects of wind speed on U-value calculation and to ensure accurate measurement of wind speed at the measurement site for the accurate calculation of the U-value. Using an anemometer or other appropriate instruments to measure wind speed at the measurement site can help ensure the accuracy of the U-value calculation. It should be noted that the weather station was

installed at the site. Due to the failure in the logger, nearby weather station data was used for the wind speed measurement.

The large deviation observed in the measurement data may be attributed to the limited number of camera calibrations performed during the entire measurement campaign. The variation in the accuracy of the IR camera over the measurement period indicates that the assumption of a constant influence of the housing temperature, as stated in section 2.2, may not hold true. The fluctuation in camera accuracy over time poses a challenge in determining the correct calibration factor. To address this issue, it is necessary to perform camera calibration for each façade while capturing images to ensure accurate and reliable results. In addition, the use of reference values, such as contact temperature sensors on each investigated surface, may improve accuracy further. Nonetheless, this approach requires a significant increase in data acquisition effort and may partially undermine the benefits of using thermal cameras for building energy analysis. Therefore, a trade-off must be made between the desired level of accuracy and the practicality of data acquisition.

The uncertainties associated with the HFM method include errors in the temperature measurements, heat flow sensors, and the heat flux transducer. Despite these uncertainties, the U-values estimated with both methods are within a reasonable range, and the drone-based IRT method provides a non-invasive and efficient means of measuring the U-values of building envelopes.

The advantages of the presented system are obvious. It has the potential to record data on insulation quality in a short time for medium-sized building complexes, e.g. office buildings, schools, or administrative headquarters, for which handheld thermography is no longer realistic, and to link this data directly to the building geometry and semantics. At present, however, it cannot exploit these advantages over normal qualitative thermography. Challenges to be solved are

- inaccurate positioning of the images and thus embedding them in the building geometry
- automated IFC-/BIM-processing regarding surfaces to be investigated, as there are significant differences in the data structure compared to CityGML [66]
- a significant improvement in the accuracy of the thermography.

In summary, the results indicate that the drone-based IRT method can provide reasonably accurate U-value estimations for building façades, but it is essential to consider the uncertainties associated with the method, particularly in wind, and camera calibration.

5 Conclusion

This thesis attempted to demonstrate the application of drone-based external IRT for the quantitative analysis of building envelope thermal performance. The methodology employed in this thesis involves the generation of a time series of surface temperature data for each individual building surface. This is achieved through the execution of multiple measurement flights conducted over the course of a single night. The aerial survey was carried out at the building complex of Hahn-Schickard in Villingen-Schwenningwen. The previous sections have outlined the advancement of the drone-based dynamic quantitative infrared thermography method. It has been demonstrated that the system, particularly its mobile application especially in combination with Building Information Models (BIM), can offer a comprehensive assessment of the thermal characteristics of the building envelope. The method provides a quick and cost-efficient solution for analyzing large surface areas using remote sensing tools. The objective of error reduction in temperature measurements by IR cameras is also handled in this thesis. The impact of camera body temperature on the accuracy of measurements was examined, and a practical approach was applied to limit the deviation of the surface temperature measurements using the blackbody correction method to estimate the correction factor described in section 4.3.

The U-values of three different façades were calculated and compared with the reference values obtained by the standard HFM method. The U-value deviation lies between 16.34 and 45.94% for three different example façades. This is in very agreement with the existing HFM and IRT-based internal measurement techniques with all the boundary conditions explained in section 3.1.2. However, measurement values scatter far more, the biggest challenge being that the measurements were largely affected by changing external environmental conditions. The most influencing parameters are the wall surface temperature and ambient reflected temperature as these parameters heavily rely on the accuracy of the IR cameras. Interestingly, the influence of the wall surface emissivity on the U-value calculation is quite low. Therefore, it can be estimated from the literature.

The key findings of this study are described as follows:

- The accuracy of the thermal sensor is influenced by environmental conditions and drone-induced wind during the flight, resulting in temperature instability and affecting the accuracy of the results.
- In the early flight images, there is greater inaccuracy compared to the mid-flight images. Over time, the deviation of temperature measurements decreases, indicating that the sensors stabilize with the environmental conditions during the flight, leading to improved accuracy of the results.

- Dynamic measurements require more frequent application of non-uniformity correction compared to stationary measurements to minimize temperature drift.
- If the problem of fluctuating accuracy of the camera cannot be solved on the hardware level, reference values in (almost) every image, e.g. contact temperature sensors on every investigated surface, might be necessary or frequent blackbody correction.
- The effects of wind speed on U-value calculation should be taken into account for accurate U-value determination. It is important to measure the wind speed and its orientation at the measurement site.
- To enable the infrared image texturing of the exterior surface, an automated flight or better GPS data might make it possible to accurately extract the position and orientation of the camera.

Nevertheless, further advancement in quantitative evaluation is necessary, considering the numerous challenges faced during data acquisition. This need is particularly significant when considering potential applications beyond the academic realm. The quality of thermographic data is highly reliant on the specific application, which makes standardization less straightforward compared to other measurement techniques.

This study made a step towards achieving a highly automated and reliable approach for inspecting and quantifying the thermal performance of building envelopes. While the utilization of unmanned aerial vehicles (UAVs) for qualitative thermal assessments of building envelopes has been extensively explored, further research is necessary to establish a robust protocol for quantitative thermal assessment. Future investigations will prioritize the development of robust protocols to enhance the accuracy of dynamic surveys. Additionally, this study highlights the limitations and offers suggestions for exploring various infrared (IR) camera technologies. It is important to emphasize that addressing these limitations necessitates further attention and investigation from both researchers and manufacturers to improve the aerial survey technology of IR cameras.

References

1. European Commission. Energy Performance of Buildings Directive. https://energy.ec.europa.eu/topics/energy-efficiency/energy-efficient-buildings/energy-performance-buildings-directive_en. Accessed 13 Dec 2022.

2. International Energy Agency. Transition to Sustainable Buildings: Strategies and opportunities to 2050. Paris: OECD/IEA; 2013.

3. Gori V. A Novel Method for the Estimation of Thermophysical Properties of Walls from Short and Seasonally Independent In-Situ Surveys [Doctoral dissertation]: University College London; 2017.

4. Byrne A, Byrne G, Davies A, Robinson AJ. Transient and Quasi-Steady Thermal Behaviour of a Building Envelope due to Retrofitted Cavity Wall and Ceiling Insulation. Energy and Buildings. 2013;61:356–65. doi:10.1016/j.enbuild.2013.02.044.

5. Hopfe CJ, Hensen JL. Uncertainty analysis in building performance simulation for design support. Energy and Buildings. 2011;43:2798–805. doi:10.1016/j.enbuild.2011.06.034.

6. Hughes M, Palmer J, Cheng V, Shipworth D. Global sensitivity analysis of England's housing energy model. Journal of Building Performance Simulation. 2015;8:283–94. doi:10.1080/19401493.2014.925505.

7. Feuermann D. Measurement of envelope thermal transmittances in multifamily buildings. Energy and Buildings. 1989;13:139–48. doi:10.1016/0378-7788(89)90005-4.

8. Fokaides PA, Kalogirou SA. Application of Infrared Thermography for the Determination of the Overall Heat Transfer Coefficient (U-Value) in Building Envelopes. Applied Energy. 2011;88:4358–65. doi:10.1016/j.apenergy.2011.05.014.

9. Tejedor B, Barreira E, Almeida RM, Casals M. Thermographic 2D U-value Map for Quantifying Thermal Bridges in Building Façades. Energy and Buildings. 2020;224:110176. doi:10.1016/j.enbuild.2020.110176.

10. Pinterić M. Building Physics. Cham: Springer International Publishing; 2017.

11. Hens H. Building Physics: Heat, Air and Moisture : Fundamentals and Engineering Methods with Examples and Exercises. 2nd ed. Berlin: Ernst & Sohn; 2012.

12. Çengel YA, Ghajar AJ. Heat and Mass Transfer: Fundamentals & applications. New York NY: McGraw-Hill Education; 2020.

13. ISO 6946: 2017. Building Components and Building Elements - Thermal Resistance and Thermal Transmittance 2017.

14. Holman J. Heat Transfer. 9th ed. Boston Mass., London: McGraw-Hill; 2002.

15. Patel D. Development and Validation of a Method to Measure the Heat-flux in Buildings using Thermography [Doctoral dissertation]. Aachen: RWTH Aachen University; to be published.

16. Usamentiaga R, Venegas P, Guerediaga J, Vega L, Molleda J, Bulnes FG. Infrared Thermography for Temperature Measurement and Non-destructive Testing. Sensors (Basel). 2014;14:12305–48. doi:10.3390/s140712305.

17. Workswell. WIRIS Pro Radiometric Inspection Thermal Camera,. https://workswell-thermal-camera.com/workswell-wiris-pro-thermal-inspection-camera-with-ultrazoom/. Accessed 20 Mar 2023.

18. Nicodemus FE, Richmond JC, Hsia JJ, Ginsberg IW, Limperis T. Geometrical Considerations and Nomenclature for Reflectance. Gaithersburg, MD: National Bureau of Standards; 1977.

19. Dochev I, Gorzalka P, Weiler V, Estevam Schmiedt J, Linkiewicz M, Eicker U, et al. Calculating Urban Heat Demands: An Analysis of two Modelling Approaches and Remote Sensing for Input Data and Validation. Energy and Buildings. 2020;226:110378. doi:10.1016/j.enbuild.2020.110378.

20. Schott JR. Methods for Estimation of and Correction for Atmospheric Effects on Remotely Sensed Data. In: Kohnle A, Miller WB, editors. Optical Engineering and Photonics in Aerospace Sensing; Sunday 11 April 1993; Orlando, FL: SPIE; 1993. p. 448–482. doi:10.1117/12.154850.

21. Transmetra. Table of Eemissivity of Various Surfaces. https://www.transmetra.ch/images/transmetra_pdf/publikationen_literatur/pyrometrie-thermografie/emissivity_table.pdf. Accessed 24 Mar 2023.

22. E07 Committee. Practice for Measuring and Compensating for Reflected Temperature Using Infrared Imaging Radiometers 2010. West Conshohocken, PA: ASTM International. doi:10.1520/E1862-97R10.

23. Baker P. U-values and traditional buildings: in situ measurements and their comparisons to calculated values. 2011. https://docslib.org/doc/1132382/technical-paper-10-u-values-and-traditional-buildings. Accessed 26 Feb 2023.

24. Li, Smith A, Biddulph P, Hamilton IG, Lowe R, Mavrogianni A, et al. Solid-Wall U-values: Heat Flux Measurements Compared with Standard Assumptions. Building Research & Information. 2015;43:238–52. doi:10.1080/09613218.2014.967977.

25. Lu X, Memari AM. Comparison of the Experimental Measurement Methods for Building Envelope Thermal Transmittance. Buildings. 2022;12:282. doi:10.3390/buildings12030282.

26. Ficco G, Iannetta F, Ianniello E, d'Ambrosio Alfano FR, Dell'Isola M. U-value in Situ Measurement for Energy Diagnosis of Existing Buildings. Energy and Buildings. 2015;104:108–21. doi:10.1016/j.enbuild.2015.06.071.

27. ISO 9869-1: 2014. Thermal insulation - Building elements - In-situ measurement of thermal resistance and thermal transmittance. Heat flow meter method 2014.

28. Hukseflux. HFP01 heat flux sensor. https://www.hukseflux.com/products/heat-flux-sensors/heat-flux-sensors/hfp01-heat-flux-sensor. Accessed 11 Jan 2023.

29. Kylili A, Fokaides PA, Christou P, Kalogirou SA. Infrared Thermography (IRT) Applications for Building Diagnostics: A review. Applied Energy. 2014;134:531–49. doi:10.1016/j.apenergy.2014.08.005.

30. Meola C, Carlomagno GM. Application of Infrared Thermography to Adhesion Science. Journal of Adhesion Science and Technology. 2006;20:589–632. doi:10.1163/156856106777412491.

31. Poblete A, Acebes Pascual M. Thermographic Measurement of the Effect of Humidity in Mortar Porosity. Infrared Physics & Technology. 2007;49:224–7. doi:10.1016/j.infrared.2006.06.009.

32. ISO 9869-2:2018. Thermal Insulation - Building Elements - In-Situ Measurement of Thermal Resistance and Thermal Transmittance - Part 2: Infrared Method for Frame Structure Dwelling 2018.

33. Fox M, Coley D, Goodhew S, Wilde P de. Time-Lapse Thermography for Building Defect Detection. Energy and Buildings. 2015;92:95–106. doi:10.1016/j.enbuild.2015.01.021.

34. Bayomi N, Nagpal S, Rakha T, Fernandez JE. Building Envelope Modeling Calibration using Aerial Thermography. Energy and Buildings. 2021;233:110648. doi:10.1016/j.enbuild.2020.110648.

35. Schott JR, Biegel JD, Wilkinson EP. Quantitative Aerial Survey Of Building Heat Loss. In: Courville GE, editor. Thermal Infrared Sensing Diagnostics; Monday 25 October 1982; Detroit: SPIE; 1983. p. 187–195. doi:10.1117/12.934479.

36. Mayer K, Haas L, Huang T, Bernabé-Moreno J, Rajagopal R, Fischer M. Estimating Building Energy Efficiency from Street View Imagery, Aerial Imagery, and Land Surface Temperature Data. Applied Energy. 2023;333:120542. doi:10.1016/j.apenergy.2022.120542.

37. Groesdonk P, Kölsch B, Patel N, Estevam Schmiedt J. Drohnenbasierte Dynamische Quantitative Infrarotthermographie in der Energetischen Analyse von Gebäuden. In: DACH-Jahrestagung 2023: DGZfP; 2023.

38. Madding R. Finding R-values of Stud Frame Constructed Houses with IR Thermography. 2008.

39. Nardi I, Paoletti D, Ambrosini D, Rubeis T de, Sfarra S. U-value Assessment by Infrared Thermography: A comparison of different calculation methods in a Guarded Hot Box. Energy and Buildings. 2016;122:211–21. doi:10.1016/j.enbuild.2016.04.017.

40. Simões I, Simões N, Tadeu A, Riachos J. Laboratory Thermal Transmittance Assessments of Homogeneous Building Elements Using Infrared Thermography. In: 2014 Quantitative InfraRed Thermography; 7-12 July, 2014: QIRT Council; 2014. doi:10.21611/qirt.2014.081.

41. ISO 18434-1:2008. Condition Monitoring and Diagnostics of Machines - Condition Monitoring and Diagnostics of Machines - Thermography - Part 1: General Procedures 2008.

42. Dall'O' G, Sarto L, Panza A. Infrared Screening of Residential Buildings for Energy Audit Purposes: Results of a Field Test. Energies. 2013;6:3859–78. doi:10.3390/en6083859.

43. Albatici R, Tonelli AM. Infrared thermovision technique for the assessment of thermal transmittance value of opaque building elements on site. Energy and Buildings. 2010;42:2177–83. doi:10.1016/j.enbuild.2010.07.010.

44. Ben H, Mackie E, Parry I, Shuckburgh E, Hawker G, Jenkins MG. Targeting Building Energy Efficiency using Thermal Infrared Earth Observation Telescopes. J. Phys.: Conf. Ser. 2021;2042:12001. doi:10.1088/1742-6596/2042/1/012001.

45. Tejedor B, Casals M, Gangolells M. Assessing the Influence of Operating Conditions and Thermophysical Properties on the Accuracy of In-Situ Measured U-values Using Quantitative Internal Infrared Thermography. Energy and Buildings. 2018;171:64–75. doi:10.1016/j.enbuild.2018.04.011.

46. Balaras CA, Argiriou AA. Infrared Thermography for Building Diagnostics. Energy and Buildings. 2002;34:171–83. doi:10.1016/S0378-7788(01)00105-0.

47. ASTM C1046-95R21. Standard Practice for In-Situ Measurement of Heat Flux and Temperature on Building Envelope Components 2021.

48. Teledyne FLIR. Infrared Camera Accuracy and Uncertainty in Plain Language. 2023. https://www.flir.com/discover/rd-science/infrared-camera-accuracy-and-uncertainty-in-plain-language/. Accessed 27 Apr 2023.

49. Agisoft. Thermal Imagery Processing. 2023. https://agisoft.freshdesk.com/support/solutions/articles/31000158942-thermal-imagery-processing. Accessed 24 May 2023.

50. Borrmann A, König M, Koch C, Beetz J, editors. Building Information Modeling. Wiesbaden: Springer Fachmedien Wiesbaden; 2015.

51. Entzian K, Scharmann R. BIM für Bauen im Bestand. In: Borrmann A, König M, Koch C, Beetz J, editors. Building Information Modeling. Wiesbaden: Springer Fachmedien Wiesbaden; 2015. p. 371–383. doi:10.1007/978-3-658-05606-3_24.

52. Rashdi R, Martínez-Sánchez J, Arias P, Qiu Z. Scanning Technologies to Building Information Modelling: A Review. Infrastructures. 2022;7:49. doi:10.3390/infrastructures7040049.

53. Pix4D. How are the Internal and External Camera Parameters defined? https://support.pix4d.com/hc/en-us/articles/202559089-How-are-the-Internal-and-External-Camera-Parameters-defined. Accessed 27 Feb 2023.

54. Frommholz D, Linkiewicz M, Poznanska AM. Inlining 3d Reconstruction, Multi-source Texture Mapping and Semantic Analysis Using Oblique Aerial Imagery. Int. Arch. Photogramm. Remote Sens. Spatial Inf. Sci. 2016;XLI-B3:605–12. doi:10.5194/isprsarchives-XLI-B3-605-2016.

55. Iwaszczuk D. Automatic Texturing of 3D Models of Urban Areas Using Image Sequences from Airborne TIR Cameras [Doctoral dissertation]. München: Technische Universität München; 2015.

56. Teledyne FLIR. What is the Typical Spectral Response for Certain Camera/Lens Combination? 2023. https://www.flir.com/support-center/Instruments/what-is-the-typical-spectral-response-for-certain-cameralens-combination/. Accessed 20 Jan 2023.

57. Minkina W, Klecha D. Atmospheric Transmission Coefficient Modelling in the Infrared for Thermovision Measurements. J. Sens. Sens. Syst. 2016;5:17–23. doi:10.5194/jsss-5-17-2016.

58. Gaussorgues G. Infrared Spectroradiometry. In: Gaussorgues G, editor. Infrared Thermography. Dordrecht: Springer Netherlands; 1994. p. 453–470. doi:10.1007/978-94-011-0711-2_15.

59. Budzier H, Gerlach G. Thermal Infrared Sensors: Theory, Optimisation, and Practice: Wiley; 2011.

60. Deutsches Zentrum für Luft- und Raumfahrt e.V. Gtom – Messsystem für Schnelle und Genaue Energetische Analysen von Gebäudehüllen für Gebäude und Quartiere. Abschlussbericht zum Forschungsvorhaben FKZ 03ET1405A. 2021. https://www.dlr.de/sf/PortalData/73/Resources/dokumente/qualifizierung/gebaeude/Gtom_Abschlussbericht.pdf. Accessed 4 Mar 2023.

61. LabIR. New Technologies Research Centre University of West Bohemia: Washable thermographic paint for special applications HEWP-LT-MWIR-BK-11. 2023. https://paints.labir.eu/homepage/thermographic-washable-paint. Accessed 2 Feb 2023.

62. Mahmoodzadeh M, Gretka V, Lee I, Mukhopadhyaya P. Infrared Thermography for Quantitative Thermal Performance Assessment of Wood-Framed Building Envelopes in Canada. Energy and Buildings. 2022;258:111807. doi:10.1016/j.enbuild.2021.111807.

63. Palyvos JA. A Survey of Wind Convection Coefficient Correlations for Building Envelope Energy Systems' Modeling. Applied Thermal Engineering. 2008;28:801–8. doi:10.1016/j.applthermaleng.2007.12.005.

64. Sharma AK, Sharma SK, Vasistha P, Mangalhara JP. Effect of Ambient Temperature on Calibration of Cooled Thermal Camera. Def. Sc. Jl. 2017;67:173. doi:10.14429/dsj.67.9820.

65. Jochum P, Lempik J, Kulka M, Blachut T, Wolff J, Wallstab T, et al. Dämmbarkeit des deutschen Gebäudebestands, Endbericht; 2015.

66. Gorzalka P, Estevam Schmiedt J, Göttsche J, Hoffschmidt B, Linkiewicz M, Patel D, et al. Remote Sensing For Building Energy Simulation Input – A Field Trial. In: Corrado V, Fabrizio E, Gasparella A, Patuzzi F, editors. Building Simulation 2019; 9/2/2019 - 9/4/2019; Rome, Italy: IBPSA; 2020. p. 4094–4101. doi:10.26868/25222708.2019.210186.

Appendix

A.1 Floor plan of Block A

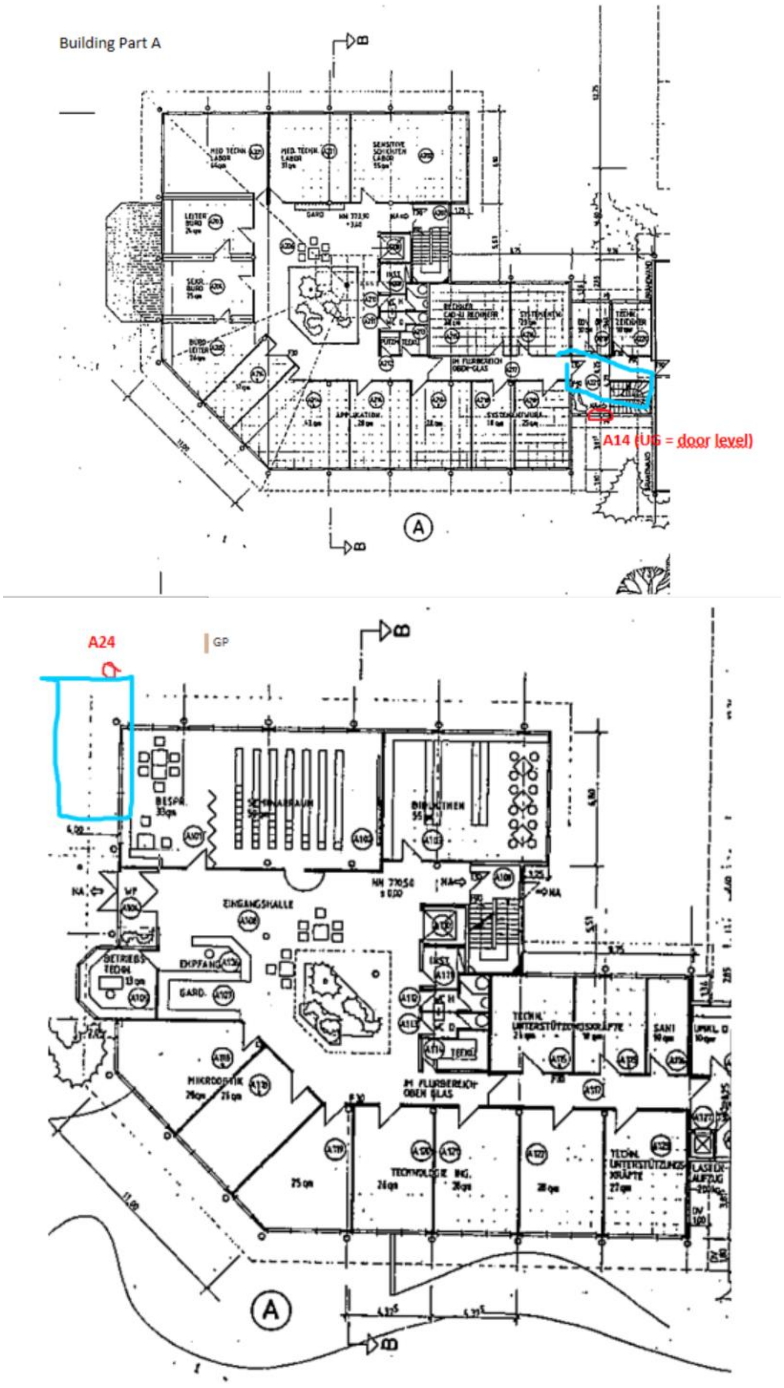

Figure 25. Floor plan of block A.

A.2 **Floor plan of Block D**

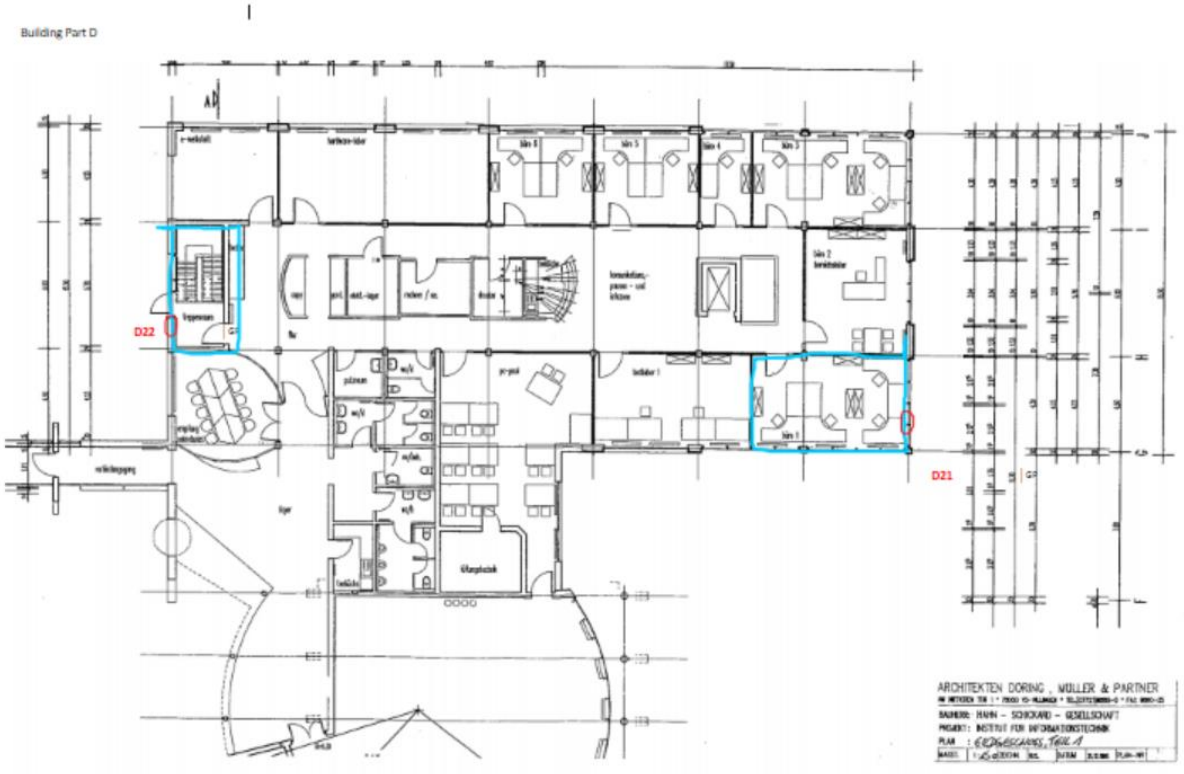

Figure 26. Floor plan of block D.

A.3 **3D Image of Block E**

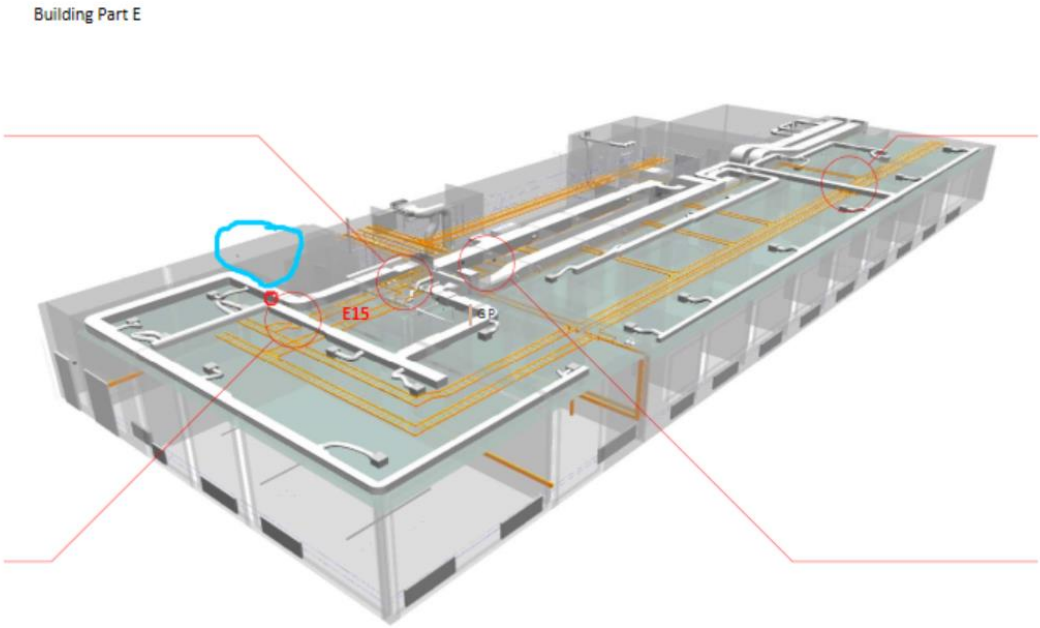

Figure 27. 3D image of block E.

A.4 **Restoring the values**

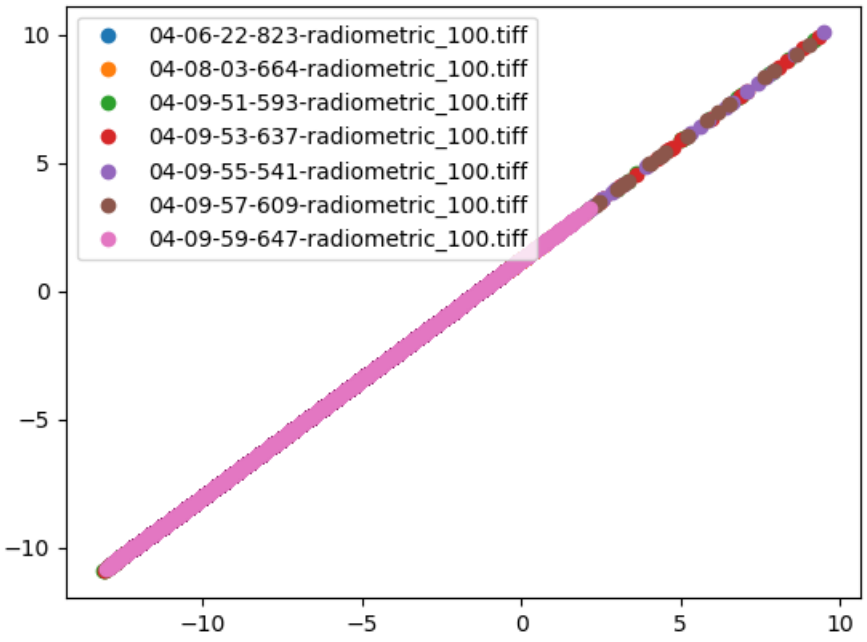

Figure 28. Mapping example image values to create a linear fit function for restoring the image values

A.5 **Passman-Larmore table**

Table 9. A part of the Passman-Larmore table for vapour absorbance α_{CO_2} [58].

Wavelength λ (μm)	P(CO2) h, mm km-1									
	0.2	0.5	1	2	5	10	20	50	100	200
7	1	1	1	1	1	1	1	1	1	1
7.1	1	1	1	1	1	1	1	1	1	1
7.2	1	1	1	1	1	1	1	1	1	1
7.3	1	1	1	1	1	1	1	1	1	1
7.4	1	1	1	1	1	1	1	1	1	1
7.5	1	1	1	1	1	1	1	1	1	1
7.6	1	1	1	1	1	1	1	1	1	1
7.7	1	1	1	1	1	1	1	1	1	1
7.8	1	1	1	1	1	1	1	1	1	1
7.9	1	1	1	1	1	1	1	1	1	1
8	1	1	1	1	1	1	1	1	1	1
8.1	1	1	1	1	1	1	1	1	1	1
8.2	1	1	1	1	1	1	1	1	1	1
8.3	1	1	1	1	1	1	1	1	1	1
8.4	1	1	1	1	1	1	1	1	1	1
8.5	1	1	1	1	1	1	1	1	1	1
8.6	1	1	1	1	1	1	1	1	1	1
8.7	1	1	1	1	1	1	1	1	1	1
8.8	1	1	1	1	1	1	1	1	1	1
8.9	1	1	1	1	1	1	1	1	1	1
9	1	1	1	1	1	1	1	1	1	1
9.1	1	1	0.999	0.999	0.998	0.995	0.991	0.978	0.955	0.914
9.2	1	1	0.999	0.998	0.995	0.991	0.982	0.955	0.913	0.834
9.3	0.999	0.997	0.995	0.99	0.975	0.951	0.904	0.776	0.605	0.363
9.4	0.993	0.982	0.965	0.931	0.837	0.7	0.491	0.168	0.028	0.001
9.5	0.993	0.983	0.967	0.935	0.842	0.715	0.512	0.187	0.035	0.001
9.6	0.996	0.99	0.98	0.961	0.906	0.821	0.675	0.363	0.14	0.029
9.7	0.995	0.986	0.973	0.947	0.873	0.761	0.58	0.256	0.065	0.004
9.8	0.997	0.992	0.984	0.969	0.924	0.858	0.73	0.455	0.206	0.043
9.9	0.998	0.995	0.989	0.979	0.948	0.897	0.811	0.585	0.342	0.123
10	1	1	0.999	0.997	0.994	0.989	0.978	0.945	0.892	0.797
10.1	1	0.999	0.998	0.996	0.99	0.98	0.96	0.902	0.814	0.663
10.2	0.997	0.994	0.988	0.977	0.943	0.89	0.792	0.558	0.312	0.097
10.3	0.997	0.994	0.987	0.975	0.939	0.881	0.777	0.532	0.283	0.08
10.4	1	1	0.999	0.998	0.995	0.991	0.982	0.955	0.913	0.834
10.5	1	1	0.999	0.998	0.998	0.995	0.991	0.978	0.955	0.914
10.6	1	1	0.999	0.999	0.998	0.995	0.991	0.978	0.955	0.914
10.7	1	1	1	0.999	0.999	0.997	0.995	0.986	0.973	0.947
10.8	1	1	0.999	0.998	0.998	0.995	0.991	0.978	0.955	0.914
10.9	1	0.999	0.999	0.997	0.993	0.986	0.973	0.934	0.872	0.761
11	1	0.999	0.999	0.997	0.993	0.986	0.973	0.934	0.872	0.761
11.1	1	0.999	0.998	0.997	0.992	0.984	0.969	0.923	0.855	0.726
11.2	1	0.999	0.998	0.995	0.989	0.978	0.955	0.892	0.796	0.633
11.3	0.999	0.999	0.997	0.994	0.985	0.971	0.942	0.862	0.742	0.552
11.4	0.999	0.998	0.997	0.993	0.983	0.966	0.934	0.842	0.709	0.503
11.5	0.999	0.998	0.996	0.992	0.98	0.96	0.921	0.814	0.661	0.438
11.6	0.999	0.998	0.995	0.991	0.977	0.955	0.912	0.794	0.632	0.399
11.7	0.999	0.998	0.995	0.991	0.977	0.955	0.912	0.794	0.632	0.399
11.8	0.999	0.998	0.997	0.993	0.983	0.966	0.934	0.842	0.709	0.503
11.9	1	0.999	0.998	0.995	0.989	0.978	0.955	0.892	0.796	0.633
12	1	1	0.999	0.999	0.997	0.993	0.986	0.966	0.934	0.872
12.1	1	1	0.999	0.998	0.998	0.995	0.991	0.978	0.955	0.914
12.2	1	1	0.999	0.998	0.998	0.995	0.991	0.978	0.955	0.914
12.3	0.998	0.995	0.99	0.981	0.952	0.907	0.823	0.614	0.376	0.142
12.4	0.994	0.985	0.97	0.941	0.859	0.738	0.545	0.218	0.048	0.002
12.5	0.987	0.968	0.936	0.877	0.719	0.517	0.268	0.037	0.001	0
12.6	0.98	0.95	0.903	0.815	0.599	0.358	0.129	0.006	0	0
12.7	0.996	0.989	0.979	0.959	0.899	0.809	0.654	0.346	0.12	0.015
12.8	0.99	0.974	0.949	0.901	0.77	0.592	0.351	0.072	0.005	0
12.9	0.985	0.962	0.925	0.856	0.677	0.458	0.21	0.02	0	0
13	0.991	0.977	0.955	0.912	0.794	0.63	0.397	0.099	0.01	0
13.1	0.99	0.974	0.949	0.9	0.768	0.592	0.348	0.071	0.005	0
13.2	0.978	0.946	0.895	0.801	0.575	0.33	0.109	0.004	0	0
13.3	0.952	0.884	0.782	0.611	0.292	0.085	0.007	0	0	0
13.4	0.935	0.846	0.715	0.512	0.187	0.035	0.001	0	0	0
13.5	0.901	0.767	0.593	0.352	0.07	0.005	0	0	0	0
13.6	0.901	0.792	0.627	0.351	0.097	0.009	0	0	0	0
13.7	0.916	0.803	0.644	0.415	0.11	0.012	0	0	0	0
13.8	0.858	0.681	0.464	0.215	0.021	0	0	0	0	0
13.9	0.778	0.534	0.286	0.082	0.002	0	0	0	0	0

Table 10. A part of the Passman-Larmore table for vapour absorbance α_{H_2O} [58].

Wavelength λ (μm)	P(H2O) h, mm km-1									
	0.2	0.5	1	2	5	10	20	50	100	200
7	0.569	0.245	0.06	0.004	0	0	0	0	0	0
7.1	0.716	0.433	0.188	0.035	0	0	0	0	0	0
7.2	0.782	0.54	0.292	0.085	0.002	0	0	0	0	0
7.3	0.849	0.664	0.441	0.194	0.017	0	0	0	0	0
7.4	0.922	0.817	0.666	0.444	0.132	0.018	0	0	0	0
7.5	0.947	0.874	0.762	0.582	0.258	0.066	0	0	0	0
7.6	0.922	0.817	0.666	0.444	0.132	0.018	0	0	0	0
7.7	0.978	0.944	0.884	0.796	0.564	0.328	0.102	0.003	0	0
7.8	0.974	0.937	0.878	0.771	0.523	0.273	0.074	0.002	0	0
7.9	0.982	0.959	0.92	0.842	0.658	0.433	0.187	0.015	0	0
8	0.99	0.975	0.951	0.904	0.777	0.603	0.365	0.08	0.006	0
8.1	0.994	0.986	0.972	0.945	0.869	0.754	0.568	0.244	0.059	0.003
8.2	0.993	0.982	0.964	0.93	0.834	0.696	0.484	0.163	0.027	0
8.3	0.995	0.988	0.976	0.953	0.887	0.786	0.618	0.3	0.09	0.008
8.4	0.995	0.987	0.975	0.95	0.88	0.774	0.599	0.278	0.077	0.006
8.5	0.994	0.986	0.972	0.944	0.866	0.75	0.562	0.237	0.056	0.003
8.6	0.996	0.992	0.982	0.965	0.915	0.837	0.702	0.411	0.169	0.029
8.7	0.996	0.992	0.983	0.966	0.916	0.839	0.704	0.416	0.173	0.03
8.8	0.997	0.993	0.983	0.966	0.917	0.841	0.707	0.421	0.177	0.031
8.9	0.997	0.992	0.983	0.966	0.918	0.843	0.709	0.425	0.18	0.032
9	0.997	0.992	0.984	0.968	0.921	0.848	0.719	0.44	0.193	0.037
9.1	0.997	0.992	0.985	0.97	0.926	0.858	0.735	0.464	0.215	0.046
9.2	0.997	0.993	0.985	0.971	0.929	0.863	0.744	0.478	0.228	0.052
9.3	0.997	0.993	0.986	0.972	0.93	0.867	0.75	0.489	0.239	0.057
9.4	0.997	0.993	0.986	0.973	0.933	0.87	0.756	0.498	0.248	0.061
9.5	0.997	0.993	0.987	0.973	0.934	0.873	0.762	0.507	0.257	0.066
9.6	0.997	0.993	0.987	0.974	0.936	0.876	0.766	0.516	0.265	0.07
9.7	0.997	0.993	0.987	0.974	0.937	0.878	0.77	0.521	0.27	0.073
9.8	0.997	0.994	0.987	0.975	0.938	0.88	0.773	0.526	0.277	0.077
9.9	0.997	0.994	0.987	0.975	0.939	0.882	0.777	0.532	0.283	0.08
10	0.998	0.994	0.988	0.975	0.94	0.883	0.78	0.538	0.289	0.083
10.1	0.998	0.994	0.988	0.975	0.94	0.883	0.78	0.538	0.289	0.083
10.2	0.998	0.994	0.988	0.975	0.94	0.883	0.78	0.538	0.289	0.083
10.3	0.998	0.994	0.988	0.976	0.94	0.884	0.781	0.54	0.292	0.085
10.4	0.998	0.994	0.988	0.976	0.941	0.885	0.782	0.542	0.294	0.086
10.5	0.998	0.994	0.988	0.976	0.941	0.886	0.784	0.544	0.295	0.087
10.6	0.998	0.994	0.988	0.976	0.942	0.887	0.786	0.548	0.3	0.089
10.7	0.948	0.994	0.988	0.976	0.942	0.887	0.787	0.55	0.302	0.091
10.8	0.998	0.994	0.988	0.976	0.941	0.886	0.784	0.544	0.295	0.087
10.9	0.998	0.994	0.988	0.976	0.94	0.884	0.781	0.54	0.292	0.085
11	0.998	0.994	0.988	0.975	0.94	0.883	0.779	0.536	0.287	0.082
11.1	0.998	0.994	0.987	0.975	0.939	0.882	0.777	0.532	0.283	0.08
11.2	0.997	0.993	0.986	0.972	0.931	0.867	0.75	0.487	0.237	0.056
11.3	0.997	0.992	0.985	0.97	0.927	0.859	0.738	0.467	0.218	0.048
11.4	0.997	0.993	0.986	0.971	0.93	0.865	0.748	0.485	0.233	0.055
11.5	0.997	0.993	0.986	0.972	0.932	0.868	0.753	0.493	0.243	0.059
11.6	0.997	0.993	0.987	0.974	0.935	0.875	0.765	0.513	0.262	0.069
11.7	0.996	0.99	0.98	0.961	0.906	0.82	0.673	0.372	0.138	0.019
11.8	0.997	0.992	0.982	0.969	0.925	0.863	0.733	0.46	0.212	0.045
11.9	0.997	0.993	0.986	0.972	0.932	0.869	0.755	0.495	0.245	0.06
12	0.997	0.993	0.987	0.974	0.937	0.878	0.77	0.521	0.27	0.073
12.1	0.997	0.994	0.987	0.975	0.938	0.88	0.773	0.526	0.277	0.077
12.2	0.997	0.994	0.987	0.975	0.938	0.88	0.775	0.528	0.279	0.078
12.3	0.997	0.993	0.987	0.974	0.937	0.878	0.77	0.521	0.27	0.073
12.4	0.997	0.993	0.987	0.974	0.935	0.874	0.764	0.511	0.261	0.068
12.5	0.997	0.993	0.986	0.973	0.933	0.871	0.759	0.502	0.252	0.063
12.6	0.997	0.993	0.986	0.972	0.931	0.868	0.752	0.491	0.241	0.058
12.7	0.997	0.993	0.985	0.971	0.929	0.863	0.744	0.478	0.228	0.052
12.8	0.997	0.992	0.985	0.97	0.926	0.858	0.736	0.466	0.217	0.047
12.9	0.997	0.993	0.984	0.969	0.924	0.853	0.728	0.452	0.204	0.041
13	0.997	0.992	0.984	0.967	0.921	0.846	0.718	0.437	0.191	0.036
13.1	0.996	0.991	0.983	0.966	0.918	0.843	0.709	0.424	0.18	0.032
13.2	0.996	0.991	0.982	0.965	0.915	0.837	0.701	0.411	0.169	0.028
13.3	0.996	0.991	0.982	0.964	0.912	0.831	0.69	0.397	0.153	0.025
13.4	0.996	0.99	0.981	0.962	0.908	0.825	0.681	0.382	0.146	0.021
13.5	0.996	0.99	0.98	0.961	0.905	0.819	0.67	0.368	0.136	0.019
13.6	0.996	0.99	0.979	0.959	0.902	0.813	0.661	0.355	0.126	0.016
13.7	0.996	0.989	0.979	0.958	0.898	0.807	0.651	0.342	0.117	0.014
13.8	0.996	0.989	0.978	0.956	0.894	0.8	0.64	0.328	0.107	0.011
13.9	0.995	0.988	0.977	0.955	0.891	0.793	0.629	0.313	0.098	0.01